

Africa's Crustal Architecture Inferred from Probabilistic and Perturbational Inversion of Ambient Noise: ADAMA

Tolulope Olugboji¹, Siyu Xue², Jean-Joel Legre¹, and Yuri Tamama^{1,3,4}

¹Department of Earth and Environmental Sciences, University of Rochester

²Georgen Institute of Data Sciences, University of Rochester

³Department of Geosciences, Princeton University

⁴Seismological Laboratory, California Institute of Technology

June 16, 2023

Abstract

Africa's continental crust hosts a variety of geologic terrains and is crucial for understanding the evolution of its longest-lived cratons. However, few of its seismic models are yet to incorporate the largest continent-wide noise dispersion datasets collected on the continent. Here, we report on new insights into Africa's crustal architecture obtained using a new dataset and model assessment product, ADAMA, which comprises a large ensemble of short period surface wave dispersion measurements. We construct a continent-wide model of **Africa's Crust Evaluated with ADAMA's Rayleigh Phase maps (ACE-ADAMA-RP)**. Phase and group dispersion maps are obtained with a probabilistic inverse modeling approach allowing us to provide constraints on uncertainty. Error statistics suggest Rayleigh phase maps are better resolved and a perturbational inverse approach based on Rayleigh waves is the basis of our update of Africa's crustal shear velocity. This model update reveals new insights into the architecture of Africa's crust not previously imaged: (1) the fastest velocities confined to the edges of the Congo craton, the west-African cratons and the Sahara Metacraton, and (2) sharp spatial gradients along craton edges, mobile belts, and within rifted margins. While most of the reported features are robust, probabilistic modeling suggests caution in interpreting features where illumination is compromised by low-quality measurements, sparse coverage or both. Future extension of our approach to other complementary seismic and geophysical datasets - e.g, multimode earthquake dispersion, receiver functions, gravity and mineral physics, will enable continent-wide lithospheric modeling that extends resolution to the upper mantle.

1 **Africa's Crustal Architecture Inferred from**
2 **Probabilistic and Perturbational Inversion of Ambient**
3 **Noise: ADAMA**

4 **Tolulope Olugboji¹, Siyu Xue^{1,2}, Jean-Joel Legre¹, Yuri Tamama^{1,3,4}**

5 ¹Department of Earth and Environmental Sciences, University of Rochester, Rochester, NY, USA

6 ²Georgen Institute of Data Sciences, University of Rochester, Rochester, NY, USA

7 ³Department of Geosciences, Princeton University, Princeton, NJ, USA

8 ⁴Seismological Laboratory, California Institute of Technology, Pasadena, CA, USA

9 **Key Points:**

- 10 • A continent-wide s-velocity model of Africa's crust is constructed using the largest
11 catalog of dispersion measurements
- 12 • The model of Africa's crust is derived from dispersion maps and error statistics ob-
13 tained from a probabilistic inverse approach
- 14 • Error statistics provide insights into the resolution and statistical significance of the
15 final model update.

Corresponding author: Tolulope Olugboji, tolugboj@ur.rochester.edu

Abstract

Africa’s continental crust hosts a variety of geologic terrains and is crucial for understanding the evolution of its longest-lived cratons. However, few of its seismic models are yet to incorporate the largest continent-wide noise dispersion datasets collected on the continent. Here, we report on new insights into Africa’s crustal architecture obtained using a new dataset and model assessment product, ADAMA, which comprises a large ensemble of short period surface wave dispersion measurements. We construct a continent-wide model of Africa’s Crust Evaluated with ADAMA’s Rayleigh Phase maps (ACE-ADAMA-RP). Phase and group dispersion maps are obtained with a probabilistic inverse modeling approach allowing us to provide constraints on uncertainty. Error statistics suggest Rayleigh phase maps are better resolved and a perturbational inverse approach based on Rayleigh waves is the basis of our update of Africa’s crustal shear velocity. This model update reveals new insights into the architecture of Africa’s crust not previously imaged: (1) the fastest velocities confined to the edges of the Congo craton, the west-African cratons and the Sahara Metacraton, and (2) sharp spatial gradients along craton edges, mobile belts, and within rifted margins. While most of the reported features are robust, probabilistic modeling suggests caution in interpreting features where illumination is compromised by low-quality measurements, sparse coverage or both. Future extension of our approach to other complementary seismic and geophysical datasets - e.g, multimode earthquake dispersion, receiver functions, gravity and mineral physics, will enable continent-wide lithospheric modeling that extends resolution to the upper mantle.

Plain Language Summary

The rocks that constitute Africa’s crust record the history of different geological periods. We produce a map, for the entire continent, of how fast shear waves travel within these rocks. We obtain this map from ambient noise surface wave vibrations. The ambient noise surface waves are generated from ocean and atmospheric waves that couple with the solid Earth. There are two types: Rayleigh and Love waves and they travel at different speeds for different wavelengths. This property is called dispersion and it is used to tell how fast the shear wave speeds travel within the subsurface rocks. Constructing the final map from ambient noise surface waves requires the solution of a computational imaging problem. We solve the most challenging computational task with a probabilistic approach – using random sampling – and this enables us to also construct associated error maps. The new maps of Africa’s crust show new features that have important implications for subsurface geology of the continent.

1 Introduction

The African continent possesses many geological terrains and tectonic features of great interest, including multiple cratons spanning billions of years in age (Begg et al., 2009; Jessell et al., 2016), a long-wavelength superswell topography in the south (Lithgow-Bertelloni & Silver, 1998; Fishwick & Bastow, 2011), active and failed continental rifts (Chorowicz, 2005; Min & Hou, 2019), hotspots and active volcanoes and multiple second-order basins and swells (Doucouré & de Wit, 2003; Burke & Gunnell, 2008)(Figure 1a). One approach to studying the diverse and spatially undersampled regions of Africa’s bulk crust is to turn to seismic velocity models (Adams & Nyblade, 2011; Pasyanos et al., 2014; Emry et al., 2019). These models provide useful constraints on the composition of the crust (Hacker et al., 2012; Rudnick & Gao, 2014; Sammon et al., 2021), the identification of structural boundaries within and across different tectonic domains (Buehler & Shearer, 2017) and how rheology (Shinevar et al., 2015, 2018) and density (Molinari & Morelli, 2011; Haas et al., 2020, 2021) influence continental rifting, isostatic and dynamic uplift, long-term deformation, and seismicity within the African plate (Behn et al., 2002; Lowry & Pérez-

65 Gussinyé, 2011; Schmandt et al., 2015; Borrego et al., 2018; Schutt et al., 2018; Fadel et al.,
66 2020; White-Gaynor et al., 2021).

67 Insight into Africa’s crust is provided by global (Laske et al., 2013; Pasyanos et al.,
68 2014), as well as continent-wide velocity models (Li & Burke, 2006; Nair et al., 2006; Yang
69 et al., 2008; Begg et al., 2009; Adams & Nyblade, 2011; Fishwick & Bastow, 2011; Fadel
70 et al., 2020). A selection of the continent-wide seismic velocity models published in the
71 last decade include Litho1.0 ((Laske et al., 2013; Pasyanos et al., 2014), Africa.ANT.Emry-
72 etal.2018 (Trabant et al., 2012; Emry et al., 2019), AF2019 (Celli, Lebedev, Schaeffer, &
73 Gaina, 2020), and SA2019 (Celli, Lebedev, Schaeffer, Ravenna, & Gaina, 2020). All of these
74 models are replicas of CRUST1.0 (Laske et al., 2013; Pasyanos et al., 2014) in the shallowest
75 crust, except for Litho1.0, a heavily cited global velocity model, which updates CRUST1.0
76 by incorporating earthquake-derived surface wave dispersion measurements, independent
77 constraints sensitive to elastic properties in the lithosphere (Laske et al., 2013; Pasyanos
78 et al., 2014). Taken together, these models incorporate both active and passive source
79 datasets, but are yet to fully integrate comprehensive ambient noise data on the continent
80 (T. Olugboji & Xue, 2022).

81 As a result, these models are limited in their resolution of Africa’s crust in two key
82 respects. First, because they do not include shortest period measurements, they lack sen-
83 sitivity to absolute velocity in the shallowest crust (Roux et al., 2005; Yang et al., 2008).
84 Second, because the continent-wide models do not include all seismic data acquisition span-
85 ning the past decade (2013-2023), (Accardo et al., 2017; Borrego et al., 2018; Emry et
86 al., 2019; Wang et al., 2019; Fadel et al., 2020; Celli, Lebedev, Schaeffer, & Gaina, 2020;
87 White-Gaynor et al., 2021), they lack spatial resolution across key tectonic domains. Here,
88 we address this and other key issues necessary for building an updated model of Africa’s
89 crust using the ambient noise dataset and model assessment product (ADAMA), provided
90 by (T. Olugboji & Xue, 2022). We use these measurements to construct continent-wide
91 Love and Rayleigh wave dispersion maps using a probabilistic approach. The inclusion of
92 short-period surface wave measurements provides improved constraints on short-wavelength
93 features, especially at the shortest periods (Lebedev et al., 2013). This allows us to provide
94 greater resolution of the shallowest crust (Figure 1b & 2a).

95 In constructing new dispersion maps, we adopt a probabilistic Bayesian approach that
96 solves for an image of surface wave speeds in the presence of irregular ray path coverage and
97 variable measurement quality (Bodin et al., 2009; Bodin, Sambridge, Tkalčić, et al., 2012;
98 Bodin & Sambridge, 2009; Bodin, Sambridge, Rawlinson, & Arroucau, 2012; T. M. Olugboji
99 et al., 2017). This technique is well suited to the dataset obtained from Africa. Furthermore,
100 it also provides information on statistical significance - that is, associated maps that quantify
101 uncertainties in the final reported dispersion maps (Bodin, Sambridge, Tkalčić, et al., 2012;
102 T. M. Olugboji et al., 2017). The dispersion maps with associated uncertainties are a useful
103 data product since they span the entire continent and can be used to assess (T. M. Olugboji
104 et al., 2017) and update existing models during linear and non-linear inversions for elastic
105 properties in the crust (Shen & Ritzwoller, 2016; Shen et al., 2016).

106 In the rest of our paper we describe, in detail, the construction of our new maps, high-
107 lighting key benefits of adopting a probabilistic Bayesian approach. We present details, not
108 yet seen before, with illumination made possible by the comprehensive ADAMA dataset. We
109 investigate the statistics and resolution present in the maps using the ensemble results ob-
110 tained from sampling the posterior distribution, comparing our results to existing published
111 results at similar periods. We provide an assessment of one of the global velocity models,
112 Litho1.0, by inverting the phase maps for depth dependent shear-wave velocity structure in
113 Africa’s crust. We discuss implications of our model for unanswered questions in Africa’s
114 tectonics and basement geology.

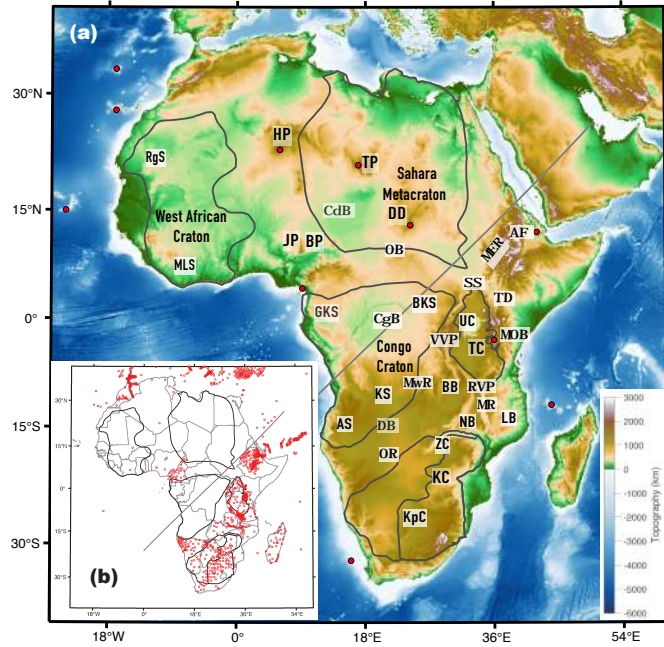


Figure 1. A broad view of Africa's geology overlaid on topography (a) The key geological tectonic features are: cratons and metacratons (gray outline), basins (low topography), hotspots (red dots). Craton outlines are from (Globig et al. 2016; Afonso et al. 2022). Abbreviations are: AF = Afar; AS = Angolan Shield; BB = Bengweulu Block; BKS = Bomu-Kibalan Shield; BP = Biu Plateau; CdB = Chad Basin; CgB = Congo Basin; CVL = Cameroon Volcanic Line; DB = Damara Belt; DD = Darfur Dome; GA = Gulf of Aden; GKS = Gabon-Kamerun Shield; HP = Hoggar Plateau; JP = Jos Plateau; KC = Kalahari Craton; KpC = Kaapvaal Craton; KS = Kasai Shield; LB = Lurio Block; MOB = Mozambique Orogenic Belt; MER = Main Ethiopian Rift; MLS = Man-Leo Shield; MR = Malawi Rift; MwR = Mweru Rift; NB = Niassa Block; OB = Oubanguides Belt; OR = Okavango Rift; Rgs = Reguibat Shield; RS = Red Sea; RVP = Rungwe Volcanic Province; SS = South Sudan; TC = Tanzania Craton; TD = Turkana Depression; TP = Tibesti Plateau; UC = Uganda Craton; VVP = Virunga Volcanic Province; ZC = Zimbabwe Craton. (b) Inset): Station distribution (red dots) used to obtain ADAMA dispersion dataset (T. Olugboji Xue 2022). Transect passing through the Congo craton and Ethiopian highlands is used to produce a 2-D vertical slice of the final crustal shear-wave velocity model after ADAMA update (see Figures 7 & 9) .

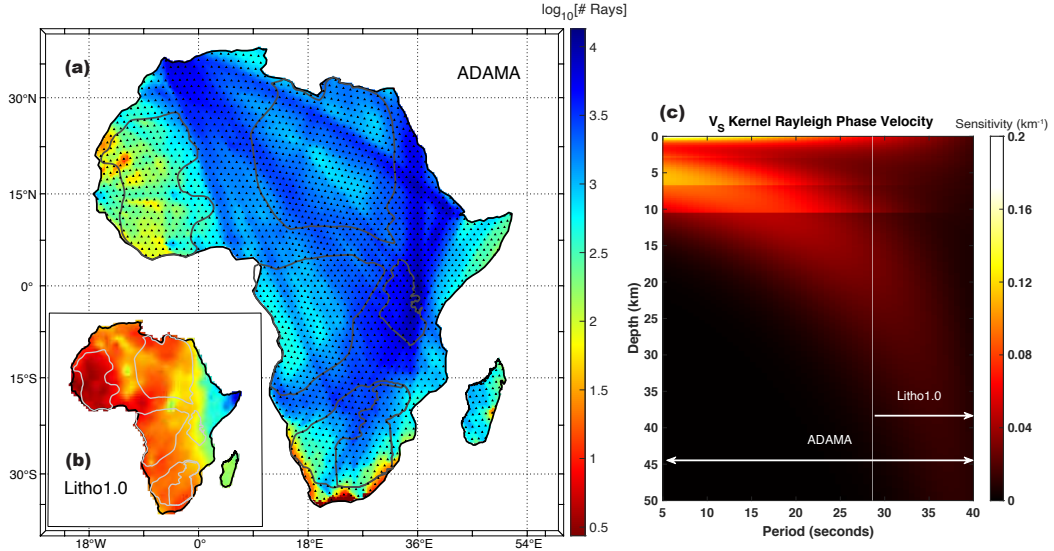


Figure 2. Shear wave sensitivity to Spatial coverage and Rayleigh wave for the ADAMA dataset. (a & b) Raypath density for the ADAMA dataset compared to a global model published in 2014 (Pasyanos et al. 2014). (c) Improved depth-sensitivity of ADAMA compared to the global Litho1.0 model showing improvements from short-period measurements.

2 Continent-wide Ambient Noise Dataset from ADAMA

The dataset used in this study - ADAMA - is from the recently published catalog of continent-wide inter-station dispersion measurements provided by (T. Olugboji & Xue, 2022). This is a large catalog of Love and Rayleigh wave phase and group dispersion measurements. The dispersion measurements are extracted from cross-spectra of continuous recordings of ambient noise ground vibrations, collected over four decades, since the commencement of digital seismometry on the continent. The inter-station cross-spectra are calculated from seismograms downloaded from 1,372 stations, spanning 62 networks in and across Africa (e.g., southern Europe, and the Middle East). The dataset spans a large collection of inter-station ray paths that provide improved spatial coverage and depth resolution of the entire continent (Figure 1b & 2a).

2.1 Love and Rayleigh Waves Dispersion with Uncertainties

For each station pair, phase and group velocities of Love and Rayleigh waves between 5 and 40 seconds are reported. Measurement uncertainty is also reported using a non-linear waveform fitting of the ambient noise cross-spectra, providing necessary regularization information during probabilistic inversion of our maps (Hawkins & Sambridge, 2019). For a detailed description of the dataset catalog, we refer the reader to (T. Olugboji & Xue, 2022). Here, we describe how improved spatial coverage and short-period measurements provide improved resolution of the crust. We also show how the entire catalog of inter-station dispersion measurements are used to obtain dispersion maps, uncertainties and shear-velocity in the entire crust.

2.2 Ray Coverage and Depth Sensitivity to Crustal Structure

The ADAMA dataset improves on global and regional surface wave dispersion catalogs in two regards: the first is increased ray-path density with better spatial sampling across the entire continent and second is that it extends the surface wave dispersion measurements to very short periods (< 25 seconds). At the shortest periods, and with rays sampling the entire continent, good resolution of the crust across the entire continent is possible (Figure 2). The new dataset reflects three orders of magnitude more measurements than the most recent continent-wide study (Emry et al., 2019).

3 Methods

3.1 Auto Adaptive & Probabilistic Noise Maps for Model Update of Africa's Crust

We construct dispersion maps by employing a probabilistic inverse approach. This approach solves for the spatial distribution of phase and group speeds, with associated uncertainties, while imposing minimal restrictions on parameterization and regularization. In Africa, where spatial sampling is highly irregular, and crustal structure is irregular, an optimal parameterization along with modeling uncertainties can still be recovered during tomographic inversion. The technique is known as transdimensional hierarchical Bayesian inversion (THBI), and has been widely used by many authors to construct surface wave dispersion maps (see (Zulfakriza et al., 2014; Galetti et al., 2016; Rawlinson et al., 2016; Crowder et al., 2019; Pilia et al., 2020)). A comprehensive discussion of THBI can be found in (Bodin et al., 2009; Bodin, Sambridge, Rawlinson, & Arroucau, 2012; Bodin, Sambridge, Tkalčić, et al., 2012). Here we provide a brief overview of the approach, show how we apply it to the ADAMA dataset, and describe how we use the maps themselves for model assessment and update of the African crust, following the statistical approach of (T. M. Olugboji et al., 2017). We do this by demonstrating that our new maps, constructed with THBI, contain information across multiple scales not yet incorporated into the continent-wide models (Pasyanos et al., 2014; Wipperfurth et al., 2020; Sammon et al., 2021). We compare model predictions of dispersion with our new probabilistic maps. Tests of statistical significance and evaluation of improved resolution are estimated using ensemble statistics. In regions of improved spatial coverage and where model predictions are different from data (dispersion maps), updates to crustal structure are obtained. We report updates, in these regions, using a perturbational inversion of our new dispersion dataset (Haney & Tsai, 2017, 2020).

3.2 Noise Maps with Transdimension Hierarchical Bayesian Inversion

The transdimensional and hierarchical Bayesian inverse approach is a class of sampling methods that seeks not just a single optimal model (dispersion maps), but rather searches the parameter space for all possible model solutions that best satisfy the observational constraints (interstation dispersion measurements). The interpretation of the ensemble of model solutions is then used to evaluate formal uncertainty. In this approach Bayesian statistics is applied to the twin challenges of model regularization and non-uniqueness. In the first part of the inversion, the transdimensional inference recognizes that the initial step of image reconstruction requires the parameterization of a 2-D surface velocity field, $\mathbf{V}(\mathbf{r})$ and this is specified by a variable number of basis (descriptor) functions and values, which are unknowns to be specified as part of the inverse solution:

$$\mathbf{V}(\mathbf{r}) = \sum_i^{N_i} v_i \mathbf{I}_i \quad (1)$$

Where the N_i velocity values, v_i , sampled at points \mathbf{r}_i are allowed to vary across the 2-D surface, thus ensuring that the velocity field is adaptively parametrized. In our imple-

181 mentation, we use a nearest-neighbor Voronoi tessellation (Figure 3a) as the basis function
 182 \mathbf{I}_i (Sambridge et al., 1995). This function tessellates the velocity field, $\mathbf{V}(\mathbf{r})$, and is widely
 183 used in transdimensional inversion (Bodin et al., 2009; Bodin, Sambridge, Rawlinson, &
 184 Arroucau, 2012); although we note here that other forms of tessellations have recently been
 185 advocated (Belhadj et al., 2018; Hawkins et al., 2019) with beneficial properties like smooth-
 186 ness.

187 In the second part of the inversion, the hierarchical inference recognizes that all inverse
 188 problems are fraught with uncertainty. That is, given the data vector of observations, \mathbf{d} ,
 189 and the model parameters $\mathbf{m} = \{v_i, r_i, N_i\}$ representing our 2-D image of the earth, errors
 190 are expected:

$$g(\mathbf{m}) = \mathbf{d} + \epsilon \quad (2)$$

191 The errors, $\epsilon = \epsilon_{data} + \epsilon_{theory} + \epsilon + \dots$, can either be due to: (1) simplifying assumptions
 192 posed by our forward modeling operator $g(\mathbf{m})$ (e.g., in our case using ray theory (Shen &
 193 Ritzwoller, 2016) instead of eikonal tomography (Lin et al., 2009; Zhou et al., 2012)), (2)
 194 observational noise which cannot be modeled even in the case of a true model $g(\mathbf{m}_{true})$, or
 195 (3) sampling and discretization errors introduced from an approximate parameterization as
 196 described in Equation 1 above. Within the Bayesian framework, the likelihood of a particular
 197 set of model predictions, are those that minimizes the probability on the prediction error
 198 term, and by definition maximizes the gaussian likelihood:

$$p(\mathbf{d}|\mathbf{m}) = \frac{1}{\prod_j \sqrt{2\pi}\sigma_j} \exp\left(-\sum_j \frac{(g(\mathbf{m})_j - \mathbf{d}_j)^2}{2\sigma_j^2}\right) \quad (3)$$

199 The standard deviation term, σ , is the hierarchical parameter, and is an additional
 200 model parameter to be solved for in the hierarchical Bayes (Malinverno & Briggs, 2004)
 201 inversion. But note that it is defined in a way so as to represent all of the sources of
 202 error present in modeling and observation, so: $\sigma_i = \sigma_{i,data} + \sigma_{theory}$. Admittedly this is
 203 a rather simplistic model, since we do not investigate covariation in measurement errors.
 204 Nonetheless, by solving for a single scaling parameter for each period, we can accommodate
 205 for this, so that:

$$\sigma_i = \lambda \sigma_{i,data} \quad (4)$$

206 In summary, a transdimensional and hierarchical Bayesian inverse solution of our noise
 207 dispersion measurements produces dispersion maps that involves sampling the posterior
 208 probability distribution for a collection of extended set of model parameters:

$$\mathbf{X} = \{\mathbf{m}, \lambda\} = \{v_i, r_i, N_i, \lambda\} \quad (5)$$

$$P(\mathbf{X}|\mathbf{d}_j = t_j^{c,u}) \propto P(\mathbf{d}_j = t_j^{c,u}|\mathbf{X})p(\mathbf{X}) \quad (6)$$

209 Where $p(\mathbf{X})$ and $P(\mathbf{d}_j = t_j^{c,u}|\mathbf{X})$ are the prior and likelihood on the extended set of
 210 model parameters \mathbf{X} (actual model parameterization, \mathbf{m} , and hierarchical uncertainties λ),
 211 \mathbf{d}_j is the data (dispersion measurements), N_j is the number of inter-station travel time
 212 measurements, for station separation, r_j , using either the interstation phase velocity, c_j or
 213 group velocity, u_j : $t_j^c = c_j/r_j$; $t_j^u = u_j/r_j$. The prior distribution is a uniform distribution,

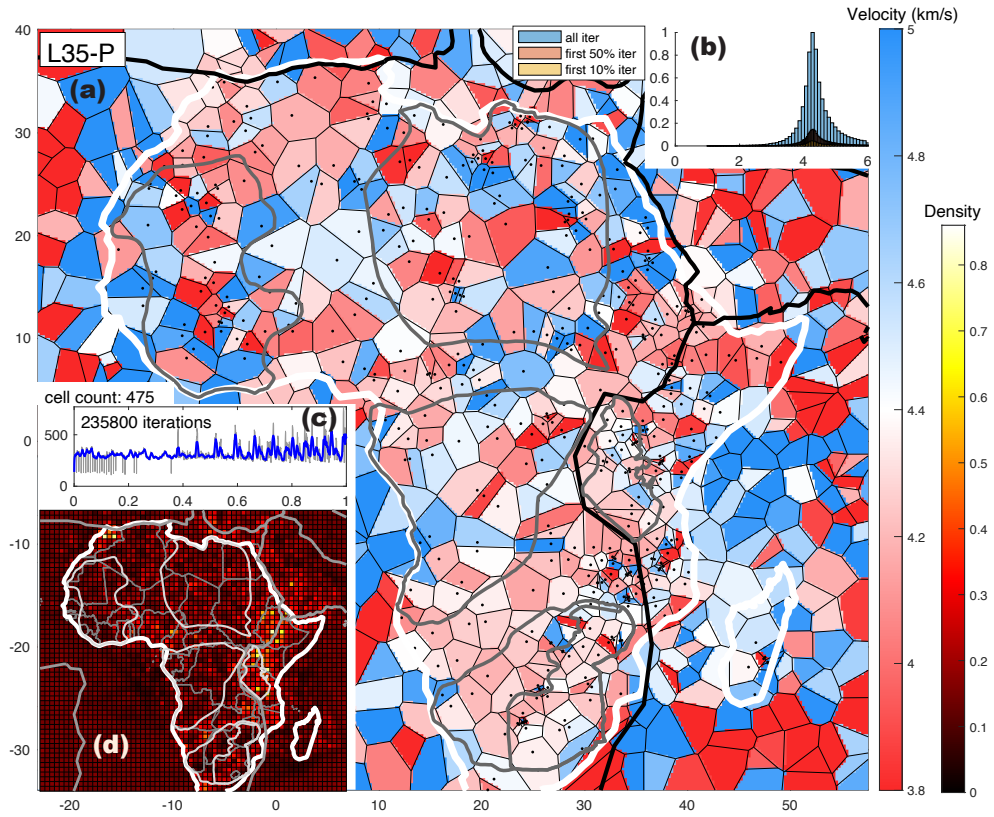


Figure 3. A snapshot through the Transdimensional Hierarchical Bayesian Inversion algorithm. (a) A single snapshot of model, \mathbf{m} , showing the irregular Voronoi tessellation used to parameterize the Love wave 2-D phase velocity map at 35 seconds. The velocity values are constant within each cell and the node centers are irregularly located in the domain (black dots). (b) The posterior distribution of the phase velocity map (blue) and after discarding the first 10% or 50% of the samples (c) A time-series tracking the total number of Voronoi cells across all parallel chains in the Monte Carlo random walk. (d) A similar statistical analysis but showing the Voronoi cell density (number of cells per pixel) across all the chains.

	Variable	Description
I. Bayesian Probabilistic Framework		
1	$P(\mathbf{X} \mathbf{d}_j = t_j^{c,u})$	Posterior distribution on model parameters \mathbf{X} , given data, \mathbf{d}
2	$p(\mathbf{X})$	Prior distribution on model parameters \mathbf{X}
3	$P(\mathbf{d}_j = t_j^{c,u} \mathbf{X})$	Likelihood of data, \mathbf{d} , given model \mathbf{X}
4	$t_j^{c,u}$	Inter-station travel time measurements
II. Transdimensional and Hierarchical Model Definition		
5	$\mathbf{X}_k = \{\mathbf{m}_k, \lambda_k\}$	A set of $3N_i + 2$ parameters for every k th McMC step
6	$\mathbf{m}_k = \{v_{ik}, r_{ik}, N_{ik}\}$	The transdimensional model parameters
7	$\mathbf{V}(\mathbf{r})$	The Voronoi tessellation for a 2-D velocity field
8	\mathbf{I}	Interpolating function that uses the Voronoi nodes
9	N_i	number of Voronoi nodes
10	λ_k	observational error for each map
11	v_{ik}^p	Phase velocities at N_i nodes
12	v_{ik}^g	Group velocities at N_i nodes
13	$\mathbf{r}_{ik} = (\theta_{ik}, \phi_{ik})$	location (longitude, latitude) of the center Voronoi nodes
III. Forward Problem and Observational Data		
14	$g(\mathbf{m})$	Forward problem predicts data given model \mathbf{X} (great circle, bezier, fast marching, etc..)
15	N_j	number of available interstation phase dispersion measurements
16	$\mathbf{d}_j = t_j^{c,u}$	data is N_j travel-time observations
17	c_j	phase dispersion measurement for stations i, j
18	u_j	group dispersion measurement for stations i, j
19	r_j	Interstation distance
IV. McMC Sampling Strategy		
20	N_c	Number of chains run in parallel
21	N_k	Number of Monte Carlo (McMC) steps per chain
22	b	No of burnin steps discarded before averaging
23	Δ_k	length of thinning steps ensures decorrelation during averaging

Table 1. A list of variables and definitions used in describing the transdimensional and hierarchical Bayesian inverse formulation

214 $p(\mathbf{X}) = \frac{1}{\beta - \alpha}$, on the set of model parameters, \mathbf{X} (in Equation 5) and is specified by identi-
 215 fying the lower and upper limits (α, β). For a summary of the most relevant parameters in
 216 the THBI process see Table 1.

217 The solution to \mathbf{X} is found by sampling the posterior distribution in Equation 6 using
 218 a reversible-jump Markov chain Monte Carlo (rj-McMC) algorithm (Green 1995). The
 219 algorithm proceeds through a random walk by perturbing an initial model \mathbf{X} to give \mathbf{X}' on
 220 every step, adding \mathbf{X}' to a collection of likely models and setting \mathbf{X}' back to \mathbf{X} if the model is
 221 accepted. Accepting (or rejecting) a proposed model is governed by acceptance probabilities
 222 that are defined in order to allow efficient sampling of the posterior distribution, and include
 223 models that, in the long run, increase the likelihood ratio of new proposed models. In this

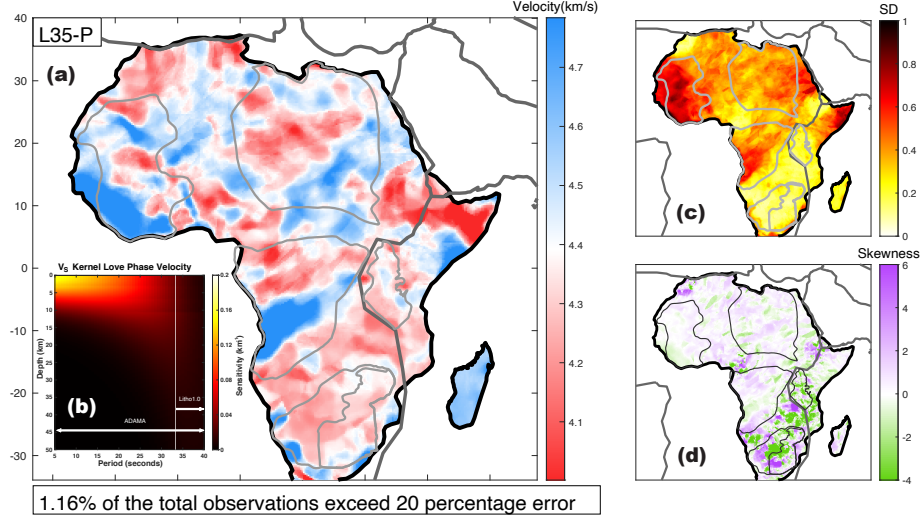


Figure 4. Statistical estimators of the posterior distribution on the 30s-Love wave phase map. (a) The mean dispersion map. (b) The sensitivity of Love waves to shear-wave velocity. (c) The standard deviation of the phase map provides an estimate of uncertainty in the phase map shown in (a) as reconstructed during the sampling of the posterior distribution. (d) A second estimator of the statistics of the posterior distribution, the skewness (second-moment) of the probability distribution showing deviation from non-gaussian statistics.

224 description, we leave the details of acceptance probabilities to the following papers for a
 225 complete discussion (Bodin et al., 2009; Hawkins et al., 2019). We point out that in the
 226 reversible jump transdimensional step, the number of model parameters, that is the set
 227 $\mathbf{m} = \{v_i, r_i, N_i\}$, is allowed to grow or shrink on every rjMCMC step. These steps are
 228 often referred to as the birth and death steps. They represent two of the four perturbation
 229 states when going from \mathbf{X} to \mathbf{X}' (Figures 3b-d). The other two perturbation states involve
 230 changing the velocity values, v_i or the hierarchical noise parameter, λ . Therefore, given a
 231 collection of N_k steps, sampled over N_c parallel chains, we obtain a final average phase or
 232 group velocity map by using the entire ensemble in \mathbf{X}_k (Figure 4a):

$$\bar{V}^{p,g}(\omega_l, \mathbf{r}) = \int_{\mathbf{m}} \mathbf{m} P(\mathbf{m}) d\mathbf{m} \approx \frac{1}{N_T} \sum_{k=b+\Delta_k}^{k=N_k \times N_c} v_{ik}^{p,g} \mathbf{I}_i(\mathbf{r}_{ik}) \quad (7)$$

233 Where the equations represents ensemble averaging using the nearest-neighbor tessella-
 234 tion of the Voronoi cells centered at longitude and latitude node coordinates $\mathbf{r}_{ik} = (\theta_{ik}, \phi_{ik})$.
 235 Whether a phase or group velocity node is implied: v_{ik}^p, v_{ik}^g , is dependent on which dataset is
 236 used, $\mathbf{d}_j = t_j^{c,u}$ (see Equation 6). During ensemble averaging, we use a total of N_T samples,
 237 discarding b burnin steps, and downsampling each chain using a thinning parameter Δ_k :

$$N_T = N_c \times \left(\frac{N_k - b}{\Delta_k} \right) \quad (8)$$

238 We also use the ensemble and its average to compute statistical estimators of the disper-
 239 sion maps' posterior distribution: that is standard deviation or second moments (skewness)
 240 (Figure 4b-c), providing a quantitative measure of statistical significance on each solution

241 (Bodin et al., 2009; Bodin & Sambridge, 2009; Bodin, Sambridge, Rawlinson, & Arroucau,
 242 2012; T. M. Olugboji et al., 2017):

$$\xi^{p,g}(\omega_l, \mathbf{r}) = \int_m (\mathbf{m} - \bar{\mathbf{m}})^2 P(\mathbf{m}) d\mathbf{m} \approx \frac{1}{\sqrt{N_T}} \sum_{k=b+\Delta_k}^{k=N_k \times N_c} [v_{ik}^{p,g} \mathbf{I}_i(\mathbf{r}_{ik}) - \bar{V}^{p,g}]^2 \quad (9)$$

243 In one sense, the average dispersion maps are model solutions of an inverse transfor-
 244 mation g^{-1} obtained through Monte Carlo Markov chain (McMC) sampling. The McMC
 245 sampling transforms the inter-station travel-time observations, N_j data vectors, into N_R
 246 dispersion curves: $[\mathbf{d}_j = t] \xrightarrow{g^{-1} \approx P(\mathbf{X})} [\mathbf{d}_R = V^{p,g}]$. The dispersion curve at each point on
 247 the African continent can then be used to solve for an earth model, $\mathbf{m}^{\beta, \alpha, \rho}(z)$:

$$\mathbf{f}(\mathbf{m}^{\beta, \alpha, \rho}(z)) = \mathbf{d}_R \quad (10)$$

248 Where, \mathbf{f} is a non-linear forward model that maps a local 1D earth model into our data
 249 of dispersion curves \mathbf{d}_R and α, β are the compressional and shear velocities and ρ is the
 250 density, all varying with depth, z . We discuss, next, our approach to obtaining this earth
 251 model

252 3.3 Shear-Velocity Model Assessment and Update using a Perturbation 253 Method

254 We use the dispersion curves obtained from the phase velocity maps to invert for an
 255 updated earth model using a perturbational approach (Haney & Tsai, 2017). We focus
 256 on assessing the shear velocity models of the global lithospheric model of (Pasyanos et al.,
 257 2014) using the Rayleigh wave dispersion measurements alone, thus highlighting regions
 258 with large data misfits. The perturbational approach uses dispersion data obtained from
 259 Bayesian inversion to generate an updated model from a starting shear velocity model (e.g.,
 260 Litho1.0), and uses an iterative gradient descent method to solve the nonlinear forward
 261 model (Equation 10) using a modified augmented system of equations:

$$\begin{bmatrix} \mathbf{C}_d^{-1/2} \mathbf{G} \\ \mathbf{C}_m^{-1/2} \mathbf{I} \end{bmatrix} \Delta \mathbf{m}_k^\beta = \begin{bmatrix} \mathbf{C}_d^{-1/2} \Delta \mathbf{d}_k \\ \mathbf{0} \end{bmatrix} \quad (11a)$$

$$\mathbf{F}_k \Delta \mathbf{m}_k^\beta = \mathbf{D}_k \quad (11b)$$

262 b.1: Iterative solution starts with $\mathbf{m}_0^\beta : \Delta \mathbf{d}_k = \mathbf{d}_R - \mathbf{f}(\mathbf{m}_k^\beta)$

263 b.2: Solving: $\Delta \mathbf{m}_k^\beta = [\mathbf{F}_k^T \mathbf{F}_k]^{-1} \mathbf{F}_k^T \mathbf{D}_k$

264 b.3: Updating: $\mathbf{m}_{k+1}^\beta = \mathbf{m}_k^\beta + \Delta \mathbf{m}_k^\beta$

265 b.4: Repeating until: $\chi^2 = \frac{\mathbf{D}_k^T \mathbf{D}_k}{F} 1 + \epsilon$

266 Where \mathbf{m}_0^β and $\Delta \mathbf{m}_k^\beta$ are the shear wave velocity and its k -th update and \mathbf{d}_R and $\Delta \mathbf{d}_k$
 267 are the observed dispersion curves and the prediction error for each iteration (Equation 10).
 268 The stopping criterion is reached (Equation 11b.4) when the dispersion measurements are
 269 matched by the predicted data for a given number of measurements, $F = l$ and $\epsilon = 0.5$.
 270 The augmented system (Equation 11a) requires computing the sensitivity kernel \mathbf{G} , and the
 271 data and model covariance matrices, \mathbf{C}_d and \mathbf{C}_m :

$$\mathbf{C}_d = \xi^2(\omega)\mathbf{I} \quad (12a)$$

$$\mathbf{C}_m = \gamma\xi^2(\omega) \exp\left(\frac{-|z_i - z_j|}{d}\right) \quad (12b)$$

272 Data covariance is diagonal and prescribed from measurement uncertainties obtained
 273 from Bayesian inversion (Equation 9), while the full matrix representing the covariance
 274 of model parameters at depth nodes z_i and z_j is prescribed by two user-supplied factors:
 275 a smoothing distance or correlation length, d , and a scaling factor γ . These parameters
 276 prescribe some type of regularization to the model solution and weight the degree of data.

277 In model assessment, we constrain shear-wave velocity by assuming (1) that the Poisson
 278 ratio and densities of the Litho1.0 model are fixed or (2) compressional velocity and density
 279 can be estimated from shear velocity, using scaling relationships derived from empirical
 280 measurements of rock elasticities (Brocher, 2005). We then use the Rayleigh wave phase
 281 dispersion results, that is the data and uncertainties, as the constraints in producing an
 282 updated model of Africa’s Crust Evaluated with ADAMA Rayleigh Phase maps (ACE-
 283 ADAMA-RP) following the iterative scheme of Equation 11. We point out that this is just
 284 one way to use the new ADAMA dataset. In principle, we could produce a new model not
 285 tied to any a priori reference model and use all the Surface Wave dispersion maps - Love
 286 dispersion as well as Rayleigh and group velocity as well as phase velocities (ACE-ADAMA-
 287 SW). Additionally, we could adopt a similar probabilistic approach to jointly invert the
 288 surface wave dispersion datasets with other body-wave seismic measurements like receiver
 289 functions (Bodin, Sambridge, Tkalčić, et al., 2012). We defer this to future work. Here, we
 290 focus on producing a model update (ACE-ADAMA-RP) based on a reference global model
 291 (Litho1.0), so that our new dispersion maps can be benchmarked and the updated models
 292 can be evaluated in the context of statistics generated from the computationally expensive
 293 THBI algorithm.

294 4 Results

295 We summarize the THBI solutions using representative Rayleigh and Love wave phase
 296 dispersion maps discretely sampled at four periods (8, 15, 20 and 35). The full solution is
 297 archived as a digital open source model (see data acknowledgement) and represents a finer
 298 sampling at $l = 11$ periods and represents one map each for Love and Rayleigh phase and
 299 group dispersion maps for a total of forty-four maps $2 \times 2 \times 11 = 44$. We present a summary
 300 of the ensemble statistics for the entire solution in Tables 2 & 3. This summary provides
 301 a synthesis of the posterior distribution for the entire set of dispersion maps, providing
 302 insights into which regions in Africa are best resolved; that is, which regions captured by
 303 all the dispersion maps are constrained with high precision and are not biased towards
 304 unreasonably large or small velocities. Finally, we produce illustrative examples of the new
 305 model of Africa’s crustal shear-velocity model using ADAMA’s Rayleigh wave phase maps
 306 and uncertainties as constraints (ACE-ADAMA-RP).

307 4.1 THBI Solutions: Exemplary Phase Maps with Errors

308 The rj-McMC algorithm is run on ~ 20 parallel chains for a total of 1 million iterations.
 309 For each Markov chain, accepted model ensembles are downsampled every 100 steps, and
 310 the final average and standard deviation are computed to produce final maps of Love and
 311 Rayleigh wave dispersion maps. We downsample, or “thin”, the model ensemble to avoid
 312 potential biases from interdependence (Bodin et al., 2009; T. M. Olugboji et al., 2017). We
 313 show exemplary maps at four distinct periods, from the shortest to longest periods (Figures
 314 5 & 6). Dispersion maps display spatial heterogeneity that depends on wavelength: more
 315 heterogeneity at shorter periods than long periods.

Prior Distributions								
Min cell (200) Max cell (2000) initial cell (320) Min group sigma (1) Max group sigma (45)								
	Rayleigh				Love			
	σ_i		\bar{C}^R		σ_i		\bar{C}^L	
T	MIN	MAX	MIN	MAX	MIN	MAX	MIN	MAX
5	12	45	0.2	6	12	45	0.2	6
6	1	45	0.2	5.5	1	45	0.2	6
8	1	45	0.2	6	1	45	0.2	6
10	1	25	0.5	6	10	45	0.2	5.5
12	1	40	0.2	6	1	40	0.2	6
15	1	40	1	6	1	40	1	6
20	1	40	0.5	6	1	40	0.5	6
25	1	30	0.5	6	1	30	0.5	6
30	1	30	0.5	6	1	30	0.5	6
35	1	25	1	6	1	25	1	6
40	1	20	1.5	6.5	1	20	1	6.5

Posterior Distributions				
	Rayleigh		Love	
T	\bar{N}_i	\bar{C}^R	\bar{N}_i	\bar{C}^L
5	582	3.73	248*	3.92*
6	437	3.63	258	3.98
8	452	3.74	331	3.99
10	310	3.75	216	3.93
12	327	3.73	286	4.05
15	433	3.73	393	4.11
20	401	3.81	673	4.16
25	403	3.91	359*	4.21*
30	374	4.00	468	4.30
35	321	4.05	322	4.36
40	334	4.14	388	4.44

* : *not fully converged*

Table 2. Phase Velocities.

316 At the shortest periods (< 12 second) we observe faster velocities in west and central
 317 Africa than in east and southern Africa (Figures a1-d1). Similar patterns of heterogeneity
 318 are observed for Love as well as Rayleigh dispersion except that Love waves travel faster
 319 than Rayleigh waves and are more sensitive to shallow structure (compare Figures 4b to
 320 Figures 2c). This explains why the Love wave maps are more heterogeneous and more
 321 uncertain than the corresponding Rayleigh maps (compare Figures 6b1 & 5b1 and Figures
 322 6b2 & 5b2).

323 In general, the error maps show that the standard deviations are lowest at the longest
 324 periods (long wavelength image > 20 secs) and when data coverage is the highest (south

	Prior Distributions				Posterior Distributions			
	Rayleigh		Love		Rayleigh		Love	
	U_i		U_i		\bar{N}_i	U_i	\bar{N}_i	U_i
T	MIN	MAX	MIN	MAX	-	-	-	-
5	0.2	5.5	0.2	5.5	306	3.61	308	3.66
6	0.2	5.5	0.2	6	284	3.64	431	3.83
8	0.2	5.8	0.2	6	361	3.69	374	3.86
10	0.5	6	0.2	6	776	3.68	400	3.86
12	0.5	6.2	0.5	6.2	358	3.70	279	3.92
15	1	6.5	0.5	6.5	540	3.68	334	3.97
20	1.5	6.5	1.5	7	600	3.54	571	3.98
25	1.5	7	1.5	7	690	3.61	703	3.99
30	2	7	1.5	7	389	3.72	711	4.07
35	2	7.5	2	7.5	434	3.86	414	4.17
40	2	7.5	2	8	455	3.94	618	4.29

Table 3. Group Velocities.

325 east vs. west and central Africa). This pattern of high uncertainties is replicated with our
326 synthetic tests (Figure S1). We observe that the uncertainties are highest for checkerboard
327 models and when data coverage is poor, compared to long-wavelength toy models with
328 good data coverage. These results suggest that the THBI algorithm can appropriately
329 model uncertainties inherent in the measurement errors as well as those inherent in the
330 reconstruction process. Although the synthetic tests show that the greatest uncertainties
331 should be expected where the station coverage is sparse, a few more statistically significant
332 patterns are distinguishable in our results, even for poor data coverage regions e.g., along
333 the Congo craton (compares Figures 5 & 6 with Figures 2a). We use the full statistics of
334 the posterior distributions to explore these patterns and describe regions of our maps that
335 are resolved with high-precision. This is important for judging final crustal model updates.

336 4.2 Ensemble Statistics of Noise Maps: Convergence & Posterior Distribu- 337 tions

338 As we've pointed out, the spatial distribution of the standard-deviation (error maps) is
339 fundamentally governed by measurement error, as well as raypath sampling. As a result, we
340 observe that the Rayleigh maps are better resolved than the Love maps, with the noisiest
341 maps being observed at the shortest periods. This is not surprising, since horizontally
342 polarized waves are noisier at this period. We also observe that the most problematic maps
343 are the 6 and 10 second maps. We summarize the statistical property of the maps across
344 different periods by classifying each pixel in Africa based on: (1) its standard deviations
345 and (2) the amplitude of the absolute velocity relative to a 1-D reference model (ak135).
346 At each location, the dispersion maps are either precise or biased depending on these two
347 measures. For example, a phase dispersion at a particular pixel location is recovered with
348 high precision and low bias when no more than two discrete periods have standard deviations
349 that exceed 0.4 km/s and the phase velocity values are not biased towards unreasonably
350 high values ($> 40\%$ of the reference value). Based on this scheme, we classify our entire
351 domain into four categories: (1) High precision, (2) Low precision, (3) Biased, (4) Unbiased,

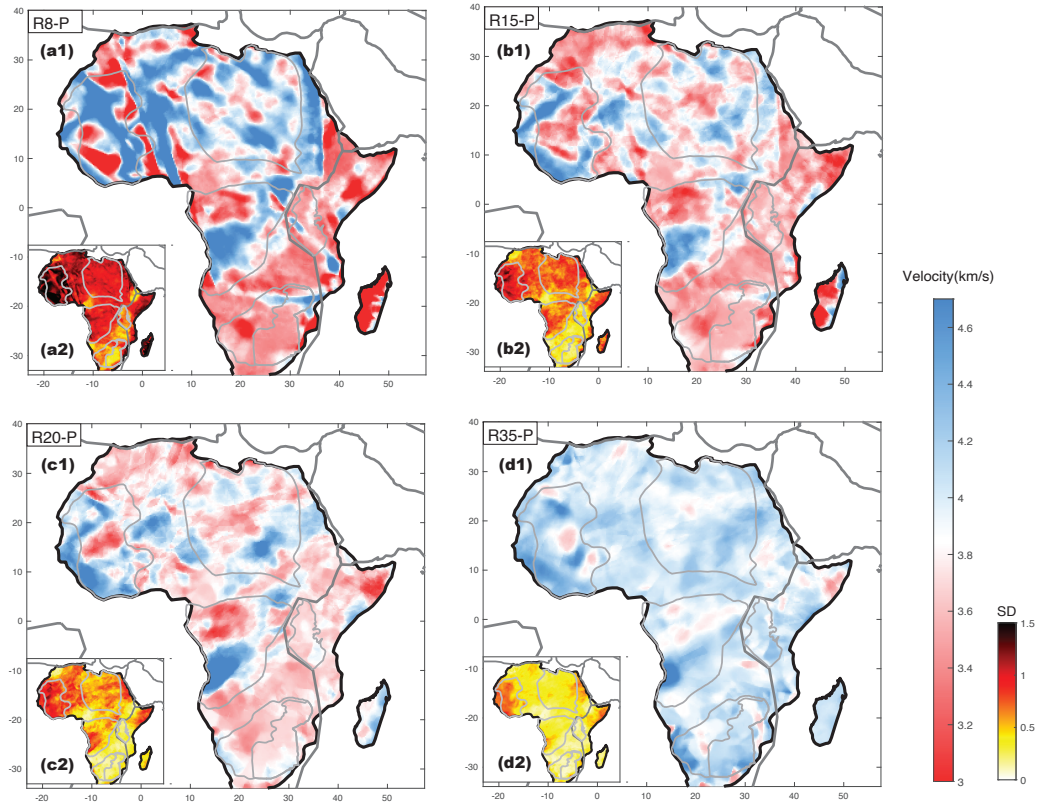


Figure 5. Rayleigh-wave phase maps and associated uncertainties at four discrete periods constructed using THBI. (a1,b1,c1,d1) Average maps constructed using the posterior distributions. (a2,b2,c2,d2) the standard deviation maps constructed using a method similar to Figure 4c. For Rayleigh wave group velocity maps see Figure S2.

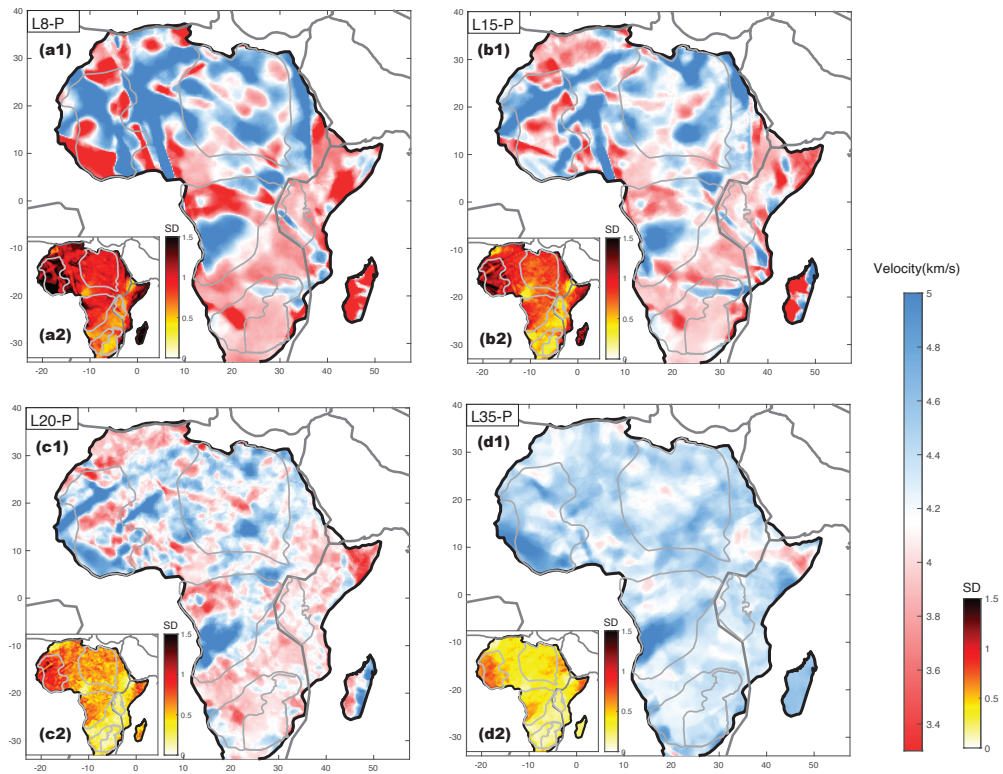


Figure 6. Same as Figure 5 but for Love-wave phase dispersion. For group velocity maps see Figure S3.

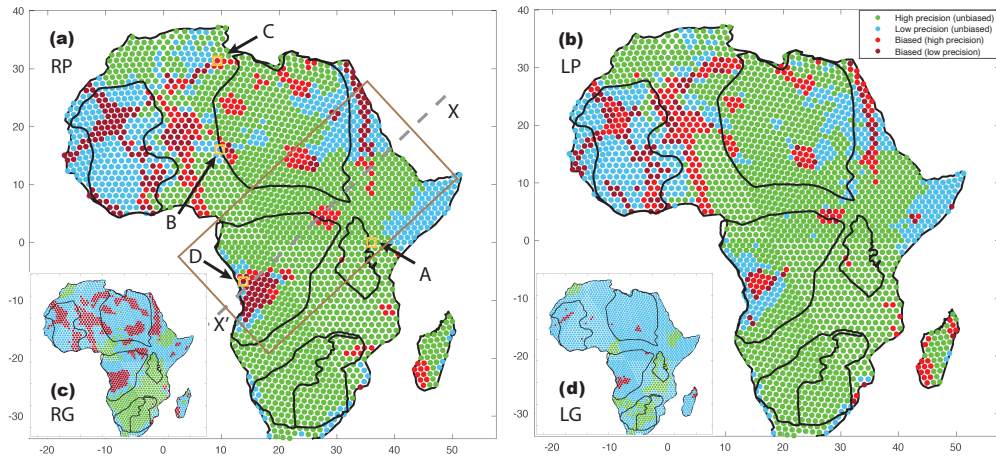


Figure 7. The quality of Rayleigh and Love dispersion models derived based on ensemble statistics. (a) The spatial statistics of Rayleigh phase dispersion is color-coded by precision and bias: high precision and unbiased (green), low precision and unbiased (blue) high-precision and biased (red), low precision and biased (brown). We identify four locations (A-B-C-D) that exemplify these four classes (b) The spatial statistics of Love phase dispersion (c) The spatial statistics of Rayleigh group dispersion (d) The spatial statistics of Love group dispersion. Model update and assessment using Rayleigh phase dispersion curves and associated uncertainties are shown at the four locations (Figure 8) and on a transect X'X crossing south-west to North-east (Figure 9).

352 each reflecting broad statistics (Figure 7). This is a comprehensive way to summarize the
 353 uncertainty inherent in our THBI solutions and how they are propagated onwards into the
 354 model update of Africa's crust.

355 We observe only a slight difference in Rayleigh and Love phase dispersion precision and
 356 bias: 64.4%, by area, for Rayleigh and 63.3%, by area, for Love. In particular, regions like
 357 Madagascar, the Sahara metacraton, the cratons of southern, central, and eastern Africa
 358 and the atlas mountains of North Africa are recovered with high precision and low bias
 359 (green dots of Figures 7a & 7b). While these regions are recovered with a high precision,
 360 some portions are highly biased. For example, the west-end of the Congo craton and the
 361 eastern edge of the Sahara meta craton. Within this large sea of 'high precision-low-bias'
 362 regions are regions on the east with low-precision-low-bias: the Horn of Africa and the
 363 western African craton (blue dots of Figures 7a & 7b). The western African craton also has
 364 the most regions with very highly biased dispersion curves (red dots of Figure 7). Again,
 365 these broad patterns are well explained by comparison with the spatial patterns of raypath
 366 coverage. Regions with the lowest precision and that are highly biased often intersect with
 367 regions of very low ray path coverage – for example, the western Africa craton, the Horn of
 368 Africa, and the eastern edge of the Congo craton (see Figure 2a).

369 Compared to the phase dispersion maps, the group dispersion maps have larger un-
 370 certainties, with only 25.3% and 13.5% by area of Rayleigh, and Love, being recovered
 371 with high precision, with large portions being recovered with very low precision and high
 372 bias (Figure 7c & 7d). While this makes it difficult to use the group dispersion results for
 373 continent-wide model assessment or update, we observe improvements in precision at some
 374 specific regions, made possible by short-aperture, country-wide seismic array deployments in
 375 Morocco, Cameroon, Ethiopia, Tanzania, and Southern Africa (T. Olugboji & Xue, 2022).
 376 For example, the cratons in the east and south of Africa are the best resolved as well as the
 377 highlands of Ethiopia, Morocco and the volcanic regions of Cameroon (compare 7c & 7d
 378 with Figure 1b). Next, the group dispersion maps for Congo craton and Sahara metacra-
 379 ton are moderately well resolved with only a few regions with highly biased values with
 380 low-precision (the western edge of the Congo craton, and a few regions in the Sahara meta
 381 craton). Finally, we observe the worst resolution for the west African craton and the mobile
 382 belts between the west african and sahara metacraton. While the group dispersion maps
 383 are not currently used in the model update, other authors may elect to use it as a constraint
 384 for investigating targeted regional crustal structure especially in highly resolved regions.
 385 For completeness, we report the entire dataset and provide the digital maps as a reference.
 386 In general, the spatial statistics of our dispersion maps shows that continent-wide model
 387 updates, using Rayleigh wave phase dispersion, are statistically significant, with room for
 388 improvement in low-resolution regions (blue and red dots of Figure 7a).

389 4.3 Africa’s Crustal Structure: Model Update and Assessment of Shear- 390 wave Velocity

391 To complete our analysis, we present a new continent-wide, shear-wave crustal velocity
 392 model of the entire African continent using the Rayleigh wave phase dispersion maps and
 393 uncertainties as a data constraint. The decision to use this dispersion dataset is predicated
 394 upon the error statistics presented in the previous section (Figure 7). An attempt to use
 395 both phase and group dispersion would lead to a final crustal model that inherits a larger set
 396 of biased and unreliable dispersion curves (Figures 7c & 7d). The new model is constructed
 397 using the Litho1.0 model as a reference starting model, therefore, we consider it both a model
 398 update as well as a model assessment product of the crust within Africa. An inversion at
 399 each grid point produces an updated 1-D model (Figure 8) that is interpolated into a quasi-
 400 3D shear velocity model which we visualize by taking 2-D vertical and horizontal projections
 401 at selected transects and depth-slices across the entire model domain. We show a few such
 402 examples selected to highlight geographic regions and crustal depths where we expect to see
 403 improvements in resolution based on better ray-path coverage and improved resolution from
 404 our short-period ADAMA catalog (Figure 2b). The 2-D projections include: (1) a vertical
 405 slice defined by a transect that runs from the western edge of the Congo craton on towards.

406 Ethiopia (Figures. 7a & 9) and (2) four horizontal slices spaced at 10-km intervals
 407 starting at the topmost crust and terminating around the Moho which is at 40 km for
 408 most of Africa (Figure 10). The vertical slice through our updated crustal model illustrates
 409 the utility of ensemble statistics. The shear-velocities are typically left unchanged when
 410 ADAMA’s Rayleigh dispersion curves do not statistically differ significantly from that of
 411 the starting reference model. Significant model updates are observed within the topmost
 412 crust (Figure 9a) informed by improved resolution at the shortest periods (Figure 2c). The
 413 updated crustal velocity model also includes uncertainties that have been forward propa-
 414 gated from the MCMC ensemble (Figure S4b). This shows that not all regions of our model
 415 update are equally well resolved. For example, along transect X’X, the shallow crust under-
 416 neath the Angolan and Bomu-Kibalan shields are the least resolved with higher standard
 417 deviations and highly biased velocities (compare Figure 7a and Figure S4b). This point is
 418 further elaborated by the four horizontal slices across the model update, ACE-ADAMA-
 419 RP, and compared with the Litho1.0 starting reference model (Figure 10). We observe the
 420 largest differences between Litho1.0 and ACE-ADAMA-RP within the top and middle crust
 421 (≤ 20 km) especially along craton edges, with our new model tending to have higher shear

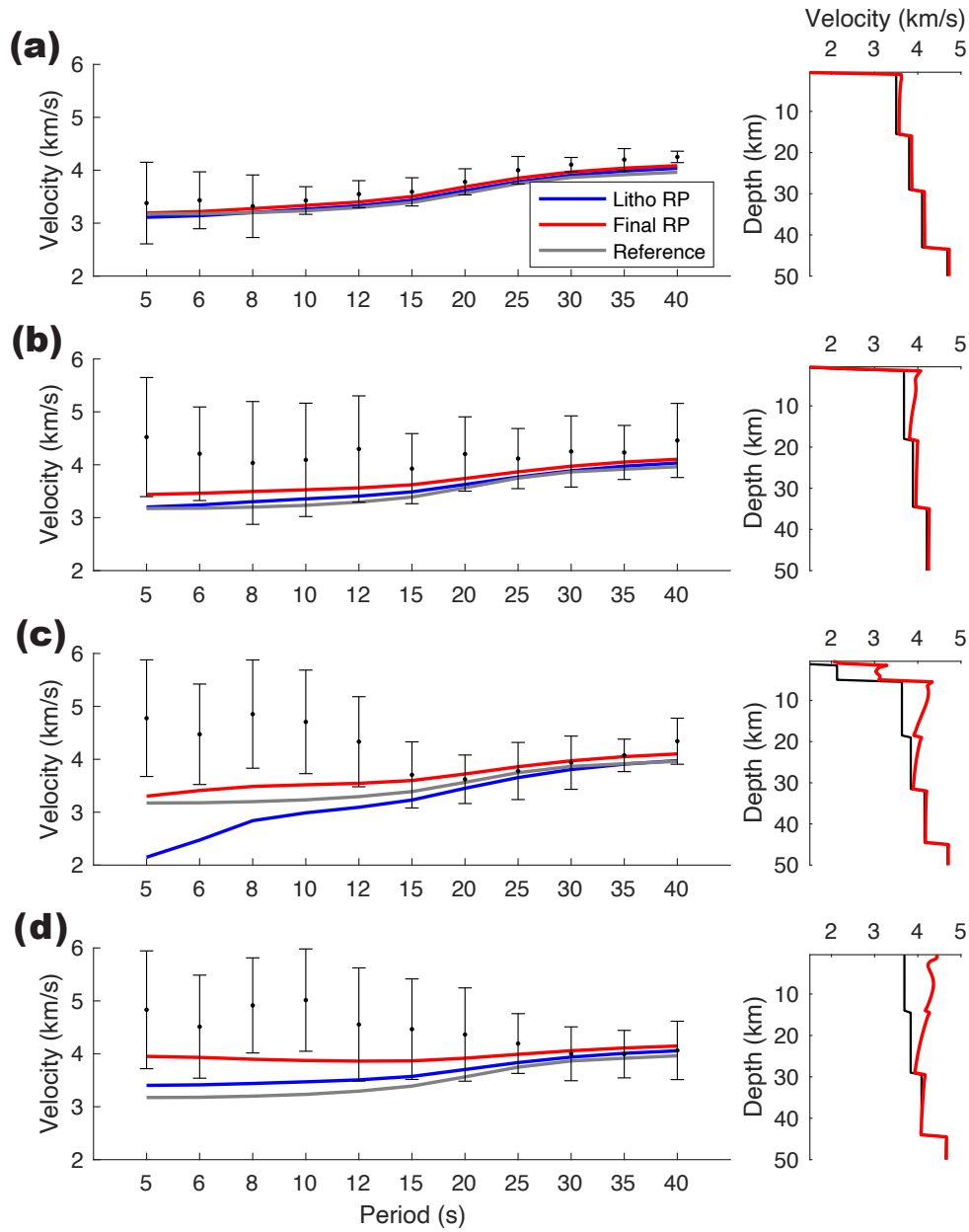


Figure 8. Illustrative examples showing model assessment and update of Litho1.0's shear-wave velocity using ADAMA's Rayleigh wave phase dispersion curve and uncertainties. Model assessment and update for: (a) a high precision and unbiased dispersion curve, starting phase velocity from Litho1.0 model (blue curve), final dispersion curve after the perturbational inversion scheme described in section 3.3 (red line) (b) a low precision and unbiased dispersion data (c) a biased and low precision data (d) a biased and high precision data. For a plot of the other predictions see Figure S2. The locations of the examples in a-d above are shown in the right map.

422 velocities compared to Litho1.0. Within the interiors of the Congo Craton and the Sahara
423 Meta Craton new features are recovered that are absent in Litho1.0. For example, the high-
424 velocity domains in the eastern edge of the Congo craton and within the North and eastern
425 end of the Sahara Meta Craton (Figure 10a-10c).

426 While some of these features are recovered from the least resolved dispersion curves
427 (high-velocity western boundaries of the western African and Congo craton), they cannot
428 be entirely explained by poor measurements since they are spatially coherent across the
429 entire crust and can be seen at the longest periods in both the Rayleigh and Love dispersion
430 measurements, which are recovered with better resolution (compare for example Figure 7
431 with Figures 4-6). The spatial extent and the reliability of these features may require further
432 tests as improvements in station coverage and data quality lead to improvements in spatial
433 resolution and lead to more precise dispersion maps.

434 5 Discussion and Interpretation

435 We have constructed a continent-wide shear velocity model of the entire African con-
436 tinent and Madagascar using a probabilistic and perturbational inversion of the most com-
437 prehensive ambient noise dispersion measurements to date (T. Olugboji & Xue, 2022). This
438 work, in Africa, is similar to other continent-wide studies that produce crustal seismic mod-
439 els based on short period passive source ambient noise seismic data (Saygin & Kennett, 2012;
440 Shen et al., 2012; Lu et al., 2018). However, in our study, we have applied the probabilistic
441 approach to constructing the ambient noise dispersion maps (Zulfakriza et al., 2014; Galetti
442 et al., 2016; Yuan & Bodin, 2018; Eshetu et al., 2021). The statistical inference facilitated by
443 a probabilistic approach has allowed us to pose, and answer, fundamental questions about
444 the statistical significance of our new dispersion results and how they inform model updates
445 of Africa’s crust (T. M. Olugboji et al., 2017): (1) at which periods are the dispersion maps
446 best resolved? (2) which regions of Africa need significant updates, and which do not? (3)
447 In the regions with improved resolution, and requiring significant model updates, to what
448 degree do existing reference models differ from current model updates based on the most
449 precise dispersion measurements i.e., Rayleigh wave phase dispersion data? Our current
450 update of Africa’s Crust (ACE-ADAMA-RP) answers all these questions, and extends our
451 understanding of Africa’s crustal architecture compared to existing ambient-noise crustal
452 models (Pasyanos et al., 2014; Emry et al., 2019; Ojo et al., 2020).

453 We reiterate that the model we have constructed here is informed primarily by the
454 vertically polarized ambient noise dispersion maps alone, and future work will explore other
455 passive source datasets like receiver functions, earthquake surface wave tomography, and
456 other seismic observables that extend resolution in the lithosphere from the crust into the
457 upper mantle (Shen et al., 2012, 2018; Gao et al., 2022; Han et al., 2022). We anticipate that
458 such future model updates will extend lateral resolution only if new datasets are collected
459 primarily in regions with the poor spatial resolution, e.g. western Africa craton (Figure
460 7). When incorporating other passive source datasets, the improved depth resolution of
461 other elastic-properties like compressional wave speed, poisson ratio, are expected only
462 when new seismic deployments overlap with low-resolution regions. For seismic methods,
463 like receiver functions, that improve sensitivity right underneath the seismic station then
464 depth resolution of crust and mantle discontinuities will only be possible when stations are
465 co-located with regions with high resolution from surface wave studies. In what follows, we
466 review the current state of seismic models of the crust (Begg et al., 2009; Crosby et al.,
467 2010; Raveloson et al., 2015; Finger et al., 2022), we contrast this with Moho models based
468 on joint inversion with other geophysical methods of obtain thermo-compositional models
469 of the African lithosphere (Globig et al., 2016; Raveloson et al., 2021; Haas et al., 2021;
470 Afonso et al., 2022).

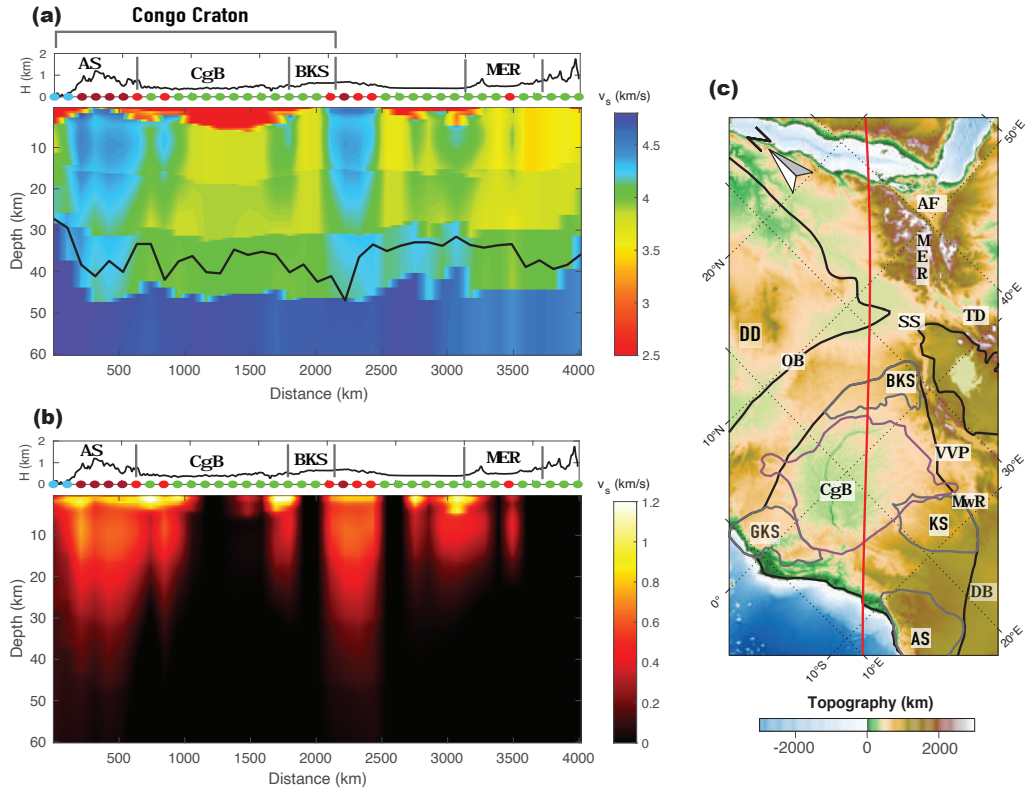


Figure 9. A vertical slice through, ACE-ADAMA-RP, the updated shear-velocity model of Africa’s Crust based on ADAMA’s Rayleigh wave phase dispersion curves. (a) The shear velocity model through transect X’X starts from the western edge of the Congo craton on towards Ethiopia (see Figure 7a). The depth to the crust-mantle boundary is shown for reference and taken from (Globig et al., 2016). (b) The difference between the final model and the starting model. (Top of 9a & 9b) Topography running through transect X’X with abbreviations same as in Figure 1a and statistical properties of each region (colored circles) same as in Figure 7a. (c) The geology surrounding transect X’X showing domains within the Congo craton, continental shield domains, the congo basin, and surrounding areas. The outline of the Congo basin is taken from (Andriamiranto Raveloson et al. 2015; A. Raveloson et al. 2021). For a view of the starting model used for the update and standard deviation of the final shear-velocity model see Figure S4a & S4b

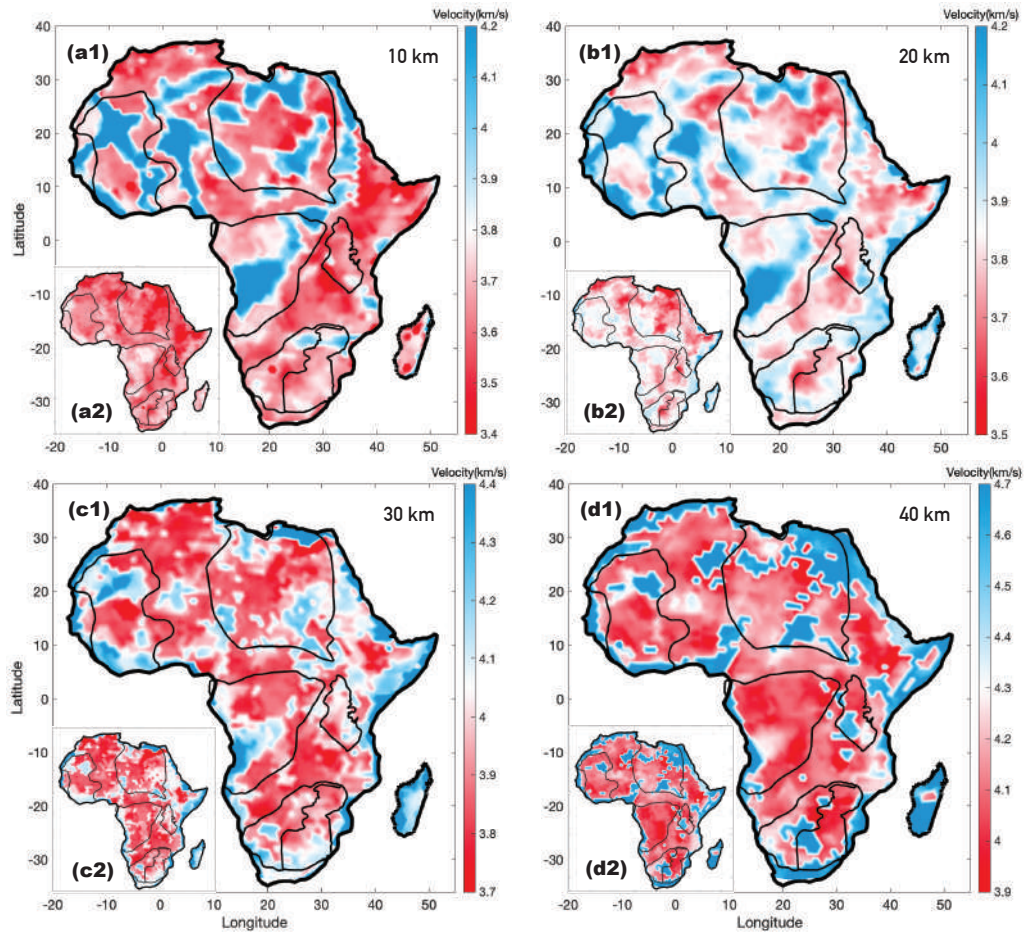


Figure 10. Horizontal slices through the updated shear-velocity model of Africa's crust. Recovered shear velocity at (a) Crustal depth of 10-km compared to Litho1.0 (b) Crustal depth of 20-km and compared to Litho1.0 (c) Crustal depth of 30-km (d) Moho and Sub-crustal depth of 40 km. All horizontal slices through the starting model of Litho1.0 are taken at the same depth as the new updated model. The transect X'X is included for reference.

471 **5.1 Comparing ADAMA to other Ambient Noise Models of Africa’s Crust**

472 A few previous studies have used ambient noise measurements to construct regional
 473 and continent-wide seismic velocity models on the continent (Yang et al., 2008; Kim et
 474 al., 2012; Pasyanos et al., 2014; Accardo et al., 2017; Borrego et al., 2018; Emry et al.,
 475 2019; Fadel et al., 2020; White-Gaynor et al., 2021). Only two of these extend across the
 476 continent providing complete crustal imaging of Africa (Pasyanos et al., 2014; Emry et al.,
 477 2019). Both studies use fewer stations and calculate dispersion measurements at periods
 478 >30 secs, therefore limiting their spatial resolution to long-wavelength features and their
 479 depth resolution to the lowermost crust and sub-moho depths (>33 km). By comparison,
 480 our work extends the resolution of crustal structure both laterally and at depth, since we
 481 extend these use a large catalog of shortest periods: 25 - 5 secs (Figure 2b) (T. Olugboji &
 482 Xue, 2022). Similar regional models (Kim et al., 2012; Borrego et al., 2018; Chambers et al.,
 483 2019; Wang et al., 2019; Fadel et al., 2020; Eshetu et al., 2021; White-Gaynor et al., 2021;
 484 Malory et al., 2022) do a similar job at providing improved depth and spatial resolution,
 485 but they do not allow a complete view of the continent-scale features. Unlike all the other
 486 models, however, the probabilistic approach makes it possible to use the large-ensemble
 487 statistics to judge resolvability of various features on the continent.

488 We point out that not all the features in our crustal model are well resolved. This
 489 is because of the uncertainties inherited from the dispersion measurements. While this
 490 might at first be discouraging, we note that we are able to identify and quantify the total
 491 area of the entire continent that is not well resolved (Figure 7). All in all, this provides
 492 users of our new velocity models with a quantitative judgment of how much confidence to
 493 place in the various parts of our new model update and which regions are highest priorities
 494 for continued updates as new seismic measurements are assimilated. As an example, it is
 495 clear that major updates are still required for the western African craton since only a few
 496 dispersion measurements have been made in that region of the African continent. Also,
 497 compared to the phase dispersion, the group dispersion measurements are still only useful
 498 for regional updates of the African continental crust (cf Figure 7b & 7c). We expect that
 499 future targets will include constraining radial anisotropy (Lin et al., 2010; Moschetti et
 500 al., 2010a, 2010b; Ojo et al., 2017) along regions where both Rayleigh and Love dispersion
 501 measurements are highly resolved with high precision, e.g., eastern and Southernmost Africa.

502 **5.2 ACE-ADAMA compared to other Geophysical Constraints on Africa’s** 503 **Crustal Structure**

504 Compared to other regions or the world, Africa is sparsely instrumented and therefore
 505 earlier seismic models based on combined active and passive source seismics have required
 506 extensive spatial averaging (Mooney, 2010; Fishwick & Bastow, 2011; Stolk et al., 2013;
 507 Globig et al., 2016). These are heavily spatially aliased models of the bulk velocity in the
 508 crust or it’s thickness (Moho depth) and have been conducted using several techniques that
 509 can be broadly categorized into three categories: (1) passive source seismics with sensitivity
 510 to the crust, e.g., receiver functions, ambient noise, or SS reflectivity (Pasyanos & Nyblade,
 511 2007; Rychert & Shearer, 2010; Tugume et al., 2013; Globig et al., 2016) (2) regionalized
 512 earthquake body wave tomography models with only marginal sensitivity to the crust, (Celli,
 513 Lebedev, Schaeffer, & Gaina, 2020; Boyce et al., 2021), and (3) joint gravity and seismic
 514 models (Haas et al., 2021; Finger et al., 2021, 2022). Compared to these techniques, we
 515 provide the best resolution on the bulk shear velocity in the crust. This is because our
 516 dataset includes an extensive measurement comprising small aperture regional networks
 517 (Nyblade, 2015; Fadel et al., 2018; Yu et al., 2020; T. Olugboji & Xue, 2022) and the
 518 adaptive probabilistic tomography approach based on these high-resolution ambient noise
 519 surface wave data improves resolution of the bulk velocities without imposing strict limiting
 520 assumptions on spatial averaging or smoothness (Bodin, Sambridge, Rawlinson, & Arroucau,
 521 2012; Sambridge et al., 2013; Belhadj et al., 2018).

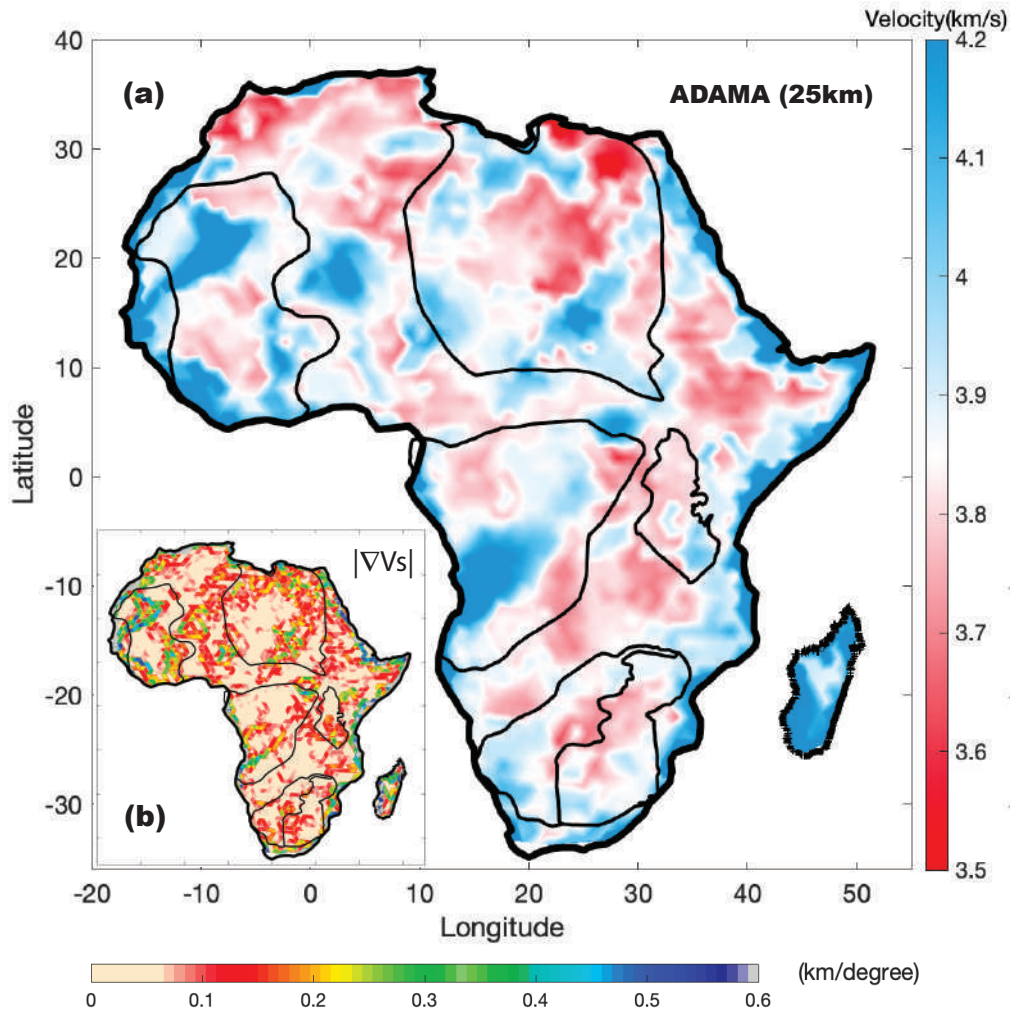


Figure 11. A view of the shear-wave velocity and its lateral gradients through the lowermost crust of Africa and Madagascar as seen by the ACE-ADAMA-RP model update. (a) The continent-wide shear wave velocities at 25 km in Africa and Madagascar. (b) The spatial gradient of the velocity field shown in (a) highlighting the regions with greatest lateral changes in shear velocities: continental margins, craton edges, and the mobile belts between WAC and SMC

5.3 Newly Resolved Features & Future Application of new Continent-wide Model

As an illustrative example of some of the newly resolved features in our new shear velocity model, we show a horizontal depth at 25 km (Figure 11). This portion of our model is constrained by highly precise Rayleigh wave dispersion measurements between 20 seconds and 35 seconds (Figures 2b, 5c2, and 4d2) and therefore the newly resolved features can be interpreted with better confidence. Compared with the reference model, Litho1.0, the shear-wave velocities are faster within the exposed Archean shields, along the continental margins, and especially for a few of the craton edges (compare Figure 10b2 with Figure 11). In particular the outlines of the Archean shields in the west African craton and the Congo craton are much more prominent and almost follow outlines predicted by the surface geology (Begg et al., 2009). The spatial homogeneity of some of these features are clearly seen in the image of the lateral gradient were the velocities hardly vary except at the edges of the shields, at the continental margins and in the highly mobile belts of between the west African craton and the Sahara Meta Craton. While these are some preliminary interpretations of the connections between the surface geology and crustal architecture revealed by our new model, we expect that future work will explore application to other geological and geophysical problems, e.g., improving constraining crustal composition (Hacker et al., 2012; Sammon et al., 2021; Sammon & McDonough, 2021; Afonso et al., 2022), lithospheric stress modeling (Zoback & Mooney, 2003; Stamps et al., 2010; Craig et al., 2011), and connection to long-term deformation and seismicity on the African continent (Schmandt et al., 2015; Fadel et al., 2020).

6 Conclusion

We construct a new shear-wave velocity model of Africa's crustal architecture using a probabilistic and perturbational inversion of ambient noise surface wave measurements. The probabilistic inversion solves for phase and group dispersion maps using a transdimensional and hierarchical Bayesian inversion of a large catalog of interstation dispersion data. The dispersion map solutions are large ensemble models of a posterior distribution and provide estimates of statistical significance. An evaluation of the error statistics suggests that the phase dispersion is better constrained than group dispersion, with Rayleigh wave phase dispersion maps possessing the best resolution. Informed by these error statistics, we use a perturbational approach to construct the updated model of Africa's crustal architecture evaluated using the Rayleigh phase maps and starting from a reference global model (Litho 1.0). The model recovers new features not present in existing maps, with important implications for crustal structure and geological architecture of Archean cratons, exposed shields and mobile belts within Africa.

7 Data Availability Statement

No seismic data was used in this study. The full catalog of dispersion measurements can be obtained from (Xue & Ologboji 2021) and was published alongside (T. Ologboji & Xue, 2022). A digital format of the probabilistic surface wave dispersion maps and the shear velocity model of Africa's Crust Evaluated using the ADAMA Rayleigh wave Phase dispersion (ACE-ADAMA-RP) is available at doi: 10.5281/zenodo.8017840.

8 Acknowledgements

This work was made possible by the National Science Foundation under grant number: 2102495. We thank the Incorporated Research Institutions for Seismology (IRIS), whose internship program allowed Tamama to pursue this research. We thank Siyu Xue, for computing the ambient noise cross correlations for all station pairs and providing us with the Love and Rayleigh wave dispersion measurements crucial to this project. We thank Baowei

570 Liu for his assistance in preparing our inversions. We thank the University of Rochester's
 571 Center for Integrated Research Computing (CIRC), for providing us with the computational
 572 support and resources for this project. We also thank Carl Schmidtman and Miki Nakajima
 573 for generously allocating us with additional computational resources. We acknowledge many
 574 helpful discussions with Lara Wagner, Baowei Liu, Ziqi Zhang, Canberk Eckmecki.

575 References

- 576 Accardo, N. J., Gaherty, J. B., Shillington, D. J., Ebinger, C. J., Nyblade, A. A., Mbogoni,
 577 G. J., ... Mruma, A. (2017, June). Surface wave imaging of the weakly extended
 578 malawi rift from ambient-noise and teleseismic rayleigh waves from onshore and lake-
 579 bottom seismometers. *Geophys. J. Int.*, *209*(3), 1892–1905.
- 580 Adams, A., & Nyblade, A. (2011, August). Shear wave velocity structure of the southern
 581 african upper mantle with implications for the uplift of southern africa. *Geophys. J.*
 582 *Int.*, *186*(2), 808–824.
- 583 Afonso, J. C., Ben-Mansour, W., O'Reilly, S. Y., Griffin, W. L., Salajegheh, F., Foley,
 584 S., ... Yang, Y. (2022, April). Thermochemical structure and evolution of cratonic
 585 lithosphere in central and southern africa. *Nat. Geosci.*, *15*(5), 405–410.
- 586 Begg, G. C., Griffin, W. L., Natapov, L. M., O'Reilly, S. Y., Grand, S. P., O'Neill, C. J.,
 587 ... Bowden, P. (2009, February). The lithospheric architecture of africa: Seismic
 588 tomography, mantle petrology, and tectonic evolution. *Geosphere*, *5*(1), 23–50.
- 589 Behn, M. D., Lin, J., & Zuber, M. T. (2002, September). A continuum mechanics model
 590 for normal faulting using a strain-rate softening rheology: implications for thermal
 591 and rheological controls on continental and oceanic rifting. *Earth Planet. Sci. Lett.*,
 592 *202*(3), 725–740.
- 593 Belhadj, J., Romary, T., Gesret, A., Noble, M., & Figliuzzi, B. (2018, May). New paramete-
 594 rizations for bayesian seismic tomography. *Inverse Probl.*, *34*(6), 065007.
- 595 Bodin, T., & Sambridge, M. (2009, September). Seismic tomography with the reversible
 596 jump algorithm. *Geophys. J. Int.*, *178*(3), 1411–1436.
- 597 Bodin, T., Sambridge, M., & Gallagher, K. (2009, March). A self-parametrizing partition
 598 model approach to tomographic inverse problems. *Inverse Probl.*, *25*(5), 055009.
- 599 Bodin, T., Sambridge, M., Rawlinson, N., & Arroucau, P. (2012, June). Transdimensional
 600 tomography with unknown data noise. *Geophys. J. Int.*, *189*(3), 1536–1556.
- 601 Bodin, T., Sambridge, M., Tkalčić, H., Arroucau, P., Gallagher, K., & Rawlinson, N. (2012).
 602 Transdimensional inversion of receiver functions and surface wave dispersion. *J. Geo-*
 603 *phys. Res. [Solid Earth]*, *117*(B2).
- 604 Borrego, D., Nyblade, A. A., Accardo, N. J., & others. (2018). Crustal structure surround-
 605 ing the northern malawi rift and beneath the rungwe volcanic province, east africa.
 606 *Geophys. J.*
- 607 Boyce, A., Bastow, I. D., Cottaar, S., Kounoudis, R., Guilloud De Courbeville, J., Caunt, E.,
 608 & Desai, S. (2021, March). AFRP20: New P -wavespeed model for the african mantle
 609 reveals two whole-mantle plumes below east africa and neoproterozoic modification of
 610 the tanzania craton. *Geochem. Geophys. Geosyst.*, *22*(3).
- 611 Brocher, T. M. (2005). Empirical relations between elastic wavespeeds and density in the
 612 earth's crust. *Bull. Seismol. Soc. Am.*, *95*(6), 2081–2092.
- 613 Buehler, J. S., & Shearer, P. M. (2017). Uppermost mantle seismic velocity structure
 614 beneath USArray. *J. Geophys. Res. [Solid Earth]*, *122*(1), 436–448.
- 615 Burke, K., & Gunnell, Y. (2008, January). The african erosion surface: A Continental-Scale
 616 synthesis of geomorphology, tectonics, and environmental. In *Memoir 201: The african*
 617 *erosion surface: A Continental-Scale synthesis of geomorphology, tectonics, and en-*
 618 *vironmental change over the past 180 million years* (Vol. 201, pp. 1–66). Geological
 619 Society of America.
- 620 Celli, N. L., Lebedev, S., Schaeffer, A. J., & Gaina, C. (2020, January). African cratonic
 621 lithosphere carved by mantle plumes. *Nat. Commun.*, *11*(1), 92.

- 622 Celli, N. L., Lebedev, S., Schaeffer, A. J., Ravenna, M., & Gaina, C. (2020, April). The upper
623 mantle beneath the south atlantic ocean, south america and africa from waveform
624 tomography with massive data sets. *Geophys. J. Int.*, *221*(1), 178–204.
- 625 Chambers, E. L., Harmon, N., Keir, D., & Rychert, C. A. (2019, April). Using ambient
626 noise to image the northern east african rift. *Geochem. Geophys. Geosyst.*, *20*(4),
627 2091–2109.
- 628 Chorowicz, J. (2005, October). The east african rift system. *J. Afr. Earth. Sci.*, *43*(1),
629 379–410.
- 630 Craig, T. J., Jackson, J. A., Priestley, K., & McKenzie, D. (2011, April). Earthquake
631 distribution patterns in africa: their relationship to variations in lithospheric and
632 geological structure, and their rheological implications. *Geophys. J. Int.*, *185*(1), 403–
633 434.
- 634 Crosby, A. G., Fishwick, S., & White, N. (2010, June). Structure and evolution of the
635 intracratonic congo basin. *Geochem. Geophys. Geosyst.*, *11*(6).
- 636 Crowder, E., Rawlinson, N., Pilia, S., Cornwell, D. G., & Reading, A. M. (2019, January).
637 Transdimensional ambient noise tomography of bass strait, southeast australia, reveals
638 the sedimentary basin and deep crustal structure beneath a failed continental rift.
639 *Geophys. J. Int.*, *217*(2), 970–987.
- 640 Doucouré, C. M., & de Wit, M. J. (2003, May). Old inherited origin for the present
641 near-bimodal topography of africa. *J. Afr. Earth. Sci.*, *36*(4), 371–388.
- 642 Emry, E. L., Shen, Y., Nyblade, A. A., Flinders, A., & Bao, X. (2019). Upper mantle earth
643 structure in africa from Full-Wave ambient noise tomography. *Geochem. Geophys.
644 Geosyst.*, *20*(1), 120–147.
- 645 Eshetu, A., Mammo, T., & Tilmann, F. (2021, November). Imaging the ethiopian rift region
646 using transdimensional hierarchical seismic noise tomography. *Pure Appl. Geophys.*,
647 *178*(11), 4367–4388.
- 648 Fadel, I., Paulssen, H., van der Meijde, M., Kwadiba, M., Ntibinyane, O., Nyblade, A.,
649 & Durrheim, R. (2020). Crustal and upper mantle shear wave velocity structure of
650 botswana: The 3 april 2017 central botswana earthquake linked to the east african
651 rift system. *Geophys. Res. Lett.*, *47*(4), e2019GL085598.
- 652 Fadel, I., van der Meijde, M., & Paulssen, H. (2018, December). Crustal structure and
653 dynamics of botswana. *J. Geophys. Res. [Solid Earth]*, *123*(12), 10,659–10,671.
- 654 Finger, N.-P., Kaban, M. K., Tesauero, M., Mooney, W. D., & Thomas, M. (2021, November).
655 *Thermo-compositional model of cratonic lithosphere and depth to moho of africa*. GFZ
656 Data Services.
- 657 Finger, N.-P., Kaban, M. K., Tesauero, M., Mooney, W. D., & Thomas, M. (2022, March). A
658 thermo-compositional model of the african cratonic lithosphere. *Geochem. Geophys.
659 Geosyst.*, *23*(3).
- 660 Fishwick, S., & Bastow, I. D. (2011, January). Towards a better understanding of african
661 topography: a review of passive-source seismic studies of the african crust and upper
662 mantle. *Geological Society, London, Special Publications*, *357*(1), 343–371.
- 663 Galetti, E., Curtis, A., Baptie, B., Jenkins, D., & Nicolson, H. (2016, August). Trans-
664 dimensional love-wave tomography of the british isles and shear-velocity structure of
665 the east irish sea basin from ambient-noise interferometry. *Geophys. J. Int.*, *208*(1),
666 36–58.
- 667 Gao, L., Zhang, H., Gao, L., He, C., Xin, H., & Shen, W. (2022, February). High-resolution
668 vs tomography of south china by joint inversion of body wave and surface wave data.
669 *Tectonophysics*, *824*, 229228.
- 670 Globig, J., Fernández, M., Torne, M., Vergés, J., Robert, A., & Faccenna, C. (2016). New
671 insights into the crust and lithospheric mantle structure of africa from elevation, geoid,
672 and thermal analysis. *J. Geophys. Res. [Solid Earth]*, *121*(7), 5389–5424.
- 673 Haas, P., Ebbing, J., Celli, N. L., & Rey, P. F. (2021). Two-step gravity inversion reveals
674 variable architecture of african cratons. *Front Earth Sci. Chin.*, *9*, 1240.
- 675 Haas, P., Ebbing, J., & Szwilius, W. (2020, June). Sensitivity analysis of gravity gradient
676 inversion of the moho depth—a case example for the amazonian craton. *Geophys. J.*

- 677 *Int.*, 221(3), 1896–1912.
- 678 Hacker, B. R., Kelemen, P. B., & Behn, M. D. (2012). Continental lower crust. *Annu. Rev.*
679 *Earth Planet. Sci.*, 43(1), 150223150959000.
- 680 Han, S., Zhang, H., Xin, H., Shen, W., & Yao, H. (2022). USTClitho2. 0: Updated unified
681 seismic tomography models for continental china lithosphere from joint inversion of
682 body-wave arrival times and surface-wave dispersion data. *Seismol. Res. Lett.*, 93(1),
683 201–215.
- 684 Haney, M. M., & Tsai, V. C. (2017). Perturbational and nonperturbational inversion of
685 rayleigh-wave velocities. , 82(3).
- 686 Haney, M. M., & Tsai, V. C. (2020, January). Perturbational and nonperturbational
687 inversion of love-wave velocities. *Geophysics*, 85(1), F19–F26.
- 688 Hawkins, R., Bodin, T., Sambridge, M., & others. (2019). Trans-Dimensional surface
689 reconstruction with different classes of parameterization. *Geochem. Explor. Environ.*
690 *Analy.*.
- 691 Hawkins, R., & Sambridge, M. (2019, July). An adjoint technique for estimation of intersta-
692 tion phase and group dispersion from ambient noise cross correlations. *Bull. Seismol.*
693 *Soc. Am.*, 109(5), 1716–1728.
- 694 Jessell, M. W., Begg, G. C., & Miller, M. S. (2016, March). The geophysical signatures of
695 the west african craton. *Precambrian Res.*, 274, 3–24.
- 696 Kim, S., Nyblade, A. A., Rhie, J., Baag, C.-E., & Kang, T.-S. (2012, November). Crustal
697 s-wave velocity structure of the main ethiopian rift from ambient noise tomography.
698 *Geophys. J. Int.*, 191(2), 865–878.
- 699 Laske, G., Masters, G., Ma, Z., & Pasyanos, M. (2013). Update on CRUST1.0 - a 1-degree
700 global model of earth’s crust. *Geophys. Res. Abstracts*, 15(Abstract EGU2013-2658).
- 701 Lebedev, S., Adam, J. M.-C., & Meier, T. (2013, December). Mapping the moho with seismic
702 surface waves: A review, resolution analysis, and recommended inversion strategies.
703 *Tectonophysics*, 609, 377–394.
- 704 Li, A., & Burke, K. (2006). Upper mantle structure of southern africa from rayleigh wave
705 tomography. *J. Geophys. Res. [Solid Earth]*, 111(B10).
- 706 Lin, F.-C., Ritzwoller, M. H., & Snieder, R. (2009, June). Eikonal tomography: surface
707 wave tomography by phase front tracking across a regional broad-band seismic array.
708 *Geophys. J. Int.*, 177(3), 1091–1110.
- 709 Lin, F.-C., Ritzwoller, M. H., Yang, Y., Moschetti, M. P., & Fouch, M. J. (2010, December).
710 Complex and variable crustal and uppermost mantle seismic anisotropy in the western
711 united states. *Nat. Geosci.*, 4(1), 55–61.
- 712 Lithgow-Bertelloni, C., & Silver, P. G. (1998, September). Dynamic topography, plate
713 driving forces and the african superswell. *Nature*, 395(6699), 269–272.
- 714 Lowry, A. R., & Pérez-Gussinyé, M. (2011, March). The role of crustal quartz in controlling
715 cordilleran deformation. *Nature*, 471(7338), 353–357.
- 716 Lu, Y., Stehly, L., & Paul, A. (2018, May). High-resolution surface wave tomography of the
717 european crust and uppermost mantle from ambient seismic noise. *Geophys. J. Int.*,
718 214(2), 1136–1150.
- 719 Malinverno, A., & Briggs, V. A. (2004, July). Expanded uncertainty quantification in inverse
720 problems: Hierarchical bayes and empirical bayes. *Geophysics*, 69(4), 1005–1016.
- 721 Malory, A. O., Bao, X., & Chen, Z. (2022, January). Crustal shear wave velocity and radial
722 anisotropy beneath southern africa from ambient noise tomography. *Tectonophysics*,
723 822, 229191.
- 724 Min, G., & Hou, G. (2019). *Mechanism of the mesozoic african rift system: Paleostress*
725 *field modeling* (Vol. 132).
- 726 Molinari, I., & Morelli, A. (2011, April). EPcrust: a reference crustal model for the european
727 plate. *Geophys. J. Int.*, 185(1), 352–364.
- 728 Mooney, W. D. (2010, January). Crust and lithospheric Structure–Global crustal structure.
729 In *Treatise on geophysics* (Vol. 1, p. 361). unknown.
- 730 Moschetti, M. P., Ritzwoller, M. H., Lin, F., & Yang, Y. (2010b). Seismic evidence
731 for widespread western-US deep-crustal deformation caused by extension. *Nature*,

- 732 464(7290), 885–889.
- 733 Moschetti, M. P., Ritzwoller, M. H., Lin, F.-C., & Yang, Y. (2010a). Crustal shear wave
734 velocity structure of the western united states inferred from ambient seismic noise and
735 earthquake data. *J. Geophys. Res.*, 115(July), 1–20.
- 736 Nair, S. K., Gao, S. S., Liu, K. H., & Silver, P. G. (2006). Southern african crustal evolution
737 and composition: Constraints from receiver function studies. *J. Geophys. Res. [Solid
738 Earth]*, 111(B2).
- 739 Nyblade, A. (2015). *Nyblade, a (2015) Africaarray-Namibia [data set]*.
- 740 Ojo, A. O., Ni, S., & Li, Z. (2017). Crustal radial anisotropy beneath cameroon from
741 ambient noise tomography. *Tectonophysics*.
- 742 Ojo, A. O., Shen, W., Ni, S., Zhao, L., Xie, J., & Kao, H. (2020, November). *Lithospheric
743 structure of africa and surrounding regions revealed by earthquake and ambient noise
744 surface wave tomography*.
- 745 Olugboji, T., & Xue, S. (2022). A Short-Period Surface-Wave dispersion dataset for model
746 assessment of africa’s crust: ADAMA. *Bull. Seismol. Soc. Am.*, 93(3), 1943–1959.
- 747 Olugboji, T. M., Lekic, V., & McDonough, W. (2017). A statistical assessment of seismic
748 models of the U.S. continental crust using bayesian inversion of ambient noise surface
749 wave dispersion data. *Tectonics*, 36(7), 1232–1253.
- 750 Pasyanos, M. E., Masters, T. G., Laske, G., & Ma, Z. (2014). LITHO1.0: An updated
751 crust and lithospheric model of the earth. *J. Geophys. Res. [Solid Earth]*, 119(3),
752 2153–2173.
- 753 Pasyanos, M. E., & Nyblade, A. A. (2007, November). A top to bottom lithospheric study
754 of africa and arabia. *Tectonophysics*, 444(1), 27–44.
- 755 Pilia, S., Jackson, J. A., Hawkins, R., Kaviani, A., & Ali, M. Y. (2020, February). The
756 southern zagros collisional orogen: New insights from transdimensional trees inversion
757 of seismic noise. *Geophys. Res. Lett.*, 47(4), e2019GL086258.
- 758 Raveloson, A., Nyblade, A., & Durrheim, R. (2021, July). Joint inversion of surface wave
759 and gravity data reveals subbasin architecture of the congo basin. *Geology*, 49(7),
760 810–815.
- 761 Raveloson, A., Nyblade, A., Fishwick, S., Mangongolo, A., & Master, S. (2015). The upper
762 mantle seismic velocity structure of South-Central africa and the seismic architecture
763 of precambrian lithosphere beneath the congo basin. In M. J. de Wit, F. Guillocheau,
764 & M. C. J. de Wit (Eds.), *Geology and resource potential of the congo basin* (pp. 3–18).
765 Berlin, Heidelberg: Springer Berlin Heidelberg.
- 766 Rawlinson, N., Pilia, S., Young, M., Salmon, M., & Yang, Y. (2016, October). Crust and
767 upper mantle structure beneath southeast australia from ambient noise and teleseismic
768 tomography. *Tectonophysics*, 689, 143–156.
- 769 Roux, P., Sabra, K. G., Kuperman, W. A., & Roux, A. (2005, January). Ambient noise
770 cross correlation in free space: Theoretical approach. *J. Acoust. Soc. Am.*, 117(1),
771 79–84.
- 772 Rudnick, R. L., & Gao, S. (2014). Composition of the continental crust. In *Treatise on
773 geochemistry* (2nd ed., Vol. 4, pp. 1–51). Elsevier.
- 774 Rychert, C. a., & Shearer, P. M. (2010, March). Resolving crustal thickness using SS
775 waveform stacks. *Geophys. J. Int.*, 180(3), 1128–1137.
- 776 Sambridge, M., Bodin, T., Gallagher, K., & Tkalcic, H. (2013, February). Transdimensional
777 inference in the geosciences. *Philos. Trans. A Math. Phys. Eng. Sci.*, 371(1984),
778 20110547.
- 779 Sambridge, M., Braun, J., & McQueen, H. (1995, December). Geophysical parametrization
780 and interpolation of irregular data using natural neighbours. *Geophys. J. Int.*, 122(3),
781 837–857.
- 782 Sammon, L. G., & McDonough, W. F. (2021, December). A geochemical review of amphi-
783 bolite, granulite, and eclogite facies lithologies: Perspectives on the deep continental
784 crust. *J. Geophys. Res. [Solid Earth]*, 126(12).
- 785 Sammon, L. G., McDonough, W. F., & Mooney, W. D. (2021, July). *The composition of
786 the deep continental crust inferred from geochemical and geophysical data*.

- 787 Saygin, E., & Kennett, B. L. N. (2012, January). Crustal structure of australia from ambient
788 seismic noise tomography. *J. Geophys. Res.*, *117*(B1).
- 789 Schmandt, B., Lin, F.-C., & Karlstrom, K. E. (2015, December). Distinct crustal isostasy
790 trends east and west of the rocky mountain front. *Geophys. Res. Lett.*, *42*(23), 10,290–
791 10,298.
- 792 Schutt, D. L., Lowry, A. R., & Buehler, J. S. (2018, March). Moho temperature and mobility
793 of lower crust in the western united states. *Geology*, *46*(3), 219–222.
- 794 Shen, W., & Ritzwoller, M. H. (2016). *Crustal and uppermost mantle structure beneath the*
795 *united states* (Vol. 121) (No. 6).
- 796 Shen, W., Ritzwoller, M. H., Kang, D., Kim, Y., Lin, F.-C., Ning, J., ... Zhou, L. (2016,
797 April). A seismic reference model for the crust and uppermost mantle beneath china
798 from surface wave dispersion. *Geophys. J. Int.*, *206*(2), 954–979.
- 799 Shen, W., Ritzwoller, M. H., Schulte-Pelkum, V., & Lin, F.-C. (2012). Joint inversion
800 of surface wave dispersion and receiver functions: a bayesian Monte-Carlo approach.
801 *Geophys. J. Int.*, *192*(2), 807–836.
- 802 Shen, W., Wiens, D. A., Anandakrishnan, S., Aster, R. C., Gerstoft, P., Bromirski, P. D., ...
803 Winberry, J. P. (2018, September). The crust and upper mantle structure of central
804 and west antarctica from bayesian inversion of rayleigh wave and receiver functions.
805 *J. Geophys. Res. [Solid Earth]*, *123*(9), 7824–7849.
- 806 Shinevar, W. J., Behn, M. D., & Hirth, G. (2015, October). Compositional dependence of
807 lower crustal viscosity. *Geophys. Res. Lett.*, *42*(20), 8333–8340.
- 808 Shinevar, W. J., Behn, M. D., Hirth, G., & Jagoutz, O. (2018, July). Inferring crustal
809 viscosity from seismic velocity: Application to the lower crust of southern california.
810 *Earth Planet. Sci. Lett.*, *494*, 83–91.
- 811 Stamps, D. S., Flesch, L. M., & Calais, E. (2010, October). Lithospheric buoyancy forces
812 in africa from a thin sheet approach. *Int. J. Earth Sci.*, *99*(7), 1525–1533.
- 813 Stolk, W., Kaban, M., Beekman, F., Tesauro, M., Mooney, W. D., & Cloetingh, S. (2013,
814 August). High resolution regional crustal models from irregularly distributed data:
815 Application to asia and adjacent areas. *Tectonophysics*, *602*, 55–68.
- 816 Trabant, C., Hutko, A. R., Bahavar, M., Karstens, R., Ahern, T., & Aster, R. (2012,
817 September). Data products at the IRIS DMC: Stepping stones for research and other
818 applications. *Seismol. Res. Lett.*, *83*(5), 846–854.
- 819 Tugume, F., Nyblade, A., Julià, J., & van der Meijde, M. (2013, December). Precam-
820 brian crustal structure in africa and arabia: Evidence lacking for secular variation.
821 *Tectonophysics*, *609*, 250–266.
- 822 Wang, T., Feng, J., Liu, K. H., & Gao, S. S. (2019, March). Crustal structure beneath the
823 malawi and luangwa rift zones and adjacent areas from ambient noise tomography.
824 *Gondwana Res.*, *67*, 187–198.
- 825 White-Gaynor, A. L., Nyblade, A. A., Durrheim, R. J., Raveloson, R., van der Meijde, M.,
826 Fadel, I., ... Sitali, M. (2021, April). Shear-wave velocity structure of the southern
827 african upper mantle: Implications for craton structure and plateau uplift. *Geophys.*
828 *Res. Lett.*, *48*(7).
- 829 Wipperfurth, S. A., Šrámek, O., & McDonough, W. F. (2020, February). Reference models
830 for lithospheric geoneutrino signal. *J. Geophys. Res. [Solid Earth]*, *125*(2).
- 831 Yang, Y., Li, A., & Ritzwoller, M. H. (2008, July). Crustal and uppermost mantle structure
832 in southern africa revealed from ambient noise and teleseismic tomography. *Geophys.*
833 *J. Int.*, *174*(1), 235–248.
- 834 Yu, Y., Gao, S. S., Zhao, D., & Liu, K. H. (2020, February). Mantle structure and
835 flow beneath an early-stage continental rift: Constraints from P wave anisotropic
836 tomography. *Tectonics*, *39*(2).
- 837 Yuan, H., & Bodin, T. (2018, July). A probabilistic shear wave velocity model of the
838 crust in the central west australian craton constrained by transdimensional inversion
839 of ambient noise dispersion. *Tectonics*, *37*(7), 1994–2012.
- 840 Zhou, L., Xie, J., Shen, W., Zheng, Y., Yang, Y., Shi, H., & Ritzwoller, M. H. (2012, June).
841 The structure of the crust and uppermost mantle beneath south china from ambient

- 842 noise and earthquake tomography. *Geophys. J. Int.*, 189(3), 1565–1583.
- 843 Zoback, M. L., & Mooney, W. D. (2003, February). Lithospheric buoyancy and continental
844 intraplate stresses. *Int. Geol. Rev.*, 45(2), 95–118.
- 845 Zulfakriza, Z., Saygin, E., Cummins, P. R., Widiyantoro, S., Nugraha, A. D., Lüher, B.-
846 G., & Bodin, T. (2014, April). Upper crustal structure of central java, indonesia,
847 from transdimensional seismic ambient noise tomography. *Geophys. J. Int.*, 197(1),
848 630–635.